

# INTERNETWORK DYNAMICS

ROBERT J. RUTTEN

*Sterrekundig Instituut, Utrecht, The Netherlands*

**Abstract.** This review places current research in quiet-Sun chromospheric dynamics in the context of past and future work, concentrating on observational aspects of three-minute oscillations and CaII  $K_{2V}$  grains. The subject is of interest at present because observations and simulations come together to permit detailed understanding of how grains form out of oscillations. Issues that remain are their spatial occurrence characteristics, in particular with respect to internetwork fields and canopies, and their energetics, in particular with respect to the basal flux.

**Key words:** Sun: chromosphere, Sun: oscillations, Sun: magnetism

## 1. Introduction

By and large, solar physics is a mature field in which progress is not so often marked by the discovery of new, unexpected phenomena, but rather by breakthroughs in understanding well-known but long-enigmatic solar behaviour. Since the Sun seems fit to offer us a plethora of fascinating structures and processes on wide ranges of temporal and spatial scales, understanding is sought in an amazing variety of solar physics subdisciplines. However, solar successes are generally scarce; not due to lack of diligence but rather to the inherent complexity, juxtaposition and interdependency of solar processes, in particular the MHD and plasma ones.

The major solar physics success stories of this century, *viz.* spectral line formation, the five-minute oscillation and the granulation, consist of and constitute photospheric radiation hydrodynamics; together, they furnish a robust view of the non-magnetic solar photosphere. Thus, it is time to move up. The point of this workshop is that chromospheric radiation hydrodynamics is ripe for a similar success story, *in casu* the dynamics of the quiet-Sun internetwork chromosphere, and that Oslo is a suitable place to say so.

In each of the three photospheric successes, confrontation between observation and numerical simulation was the key to reaching detailed understanding. The long story of numerical line formation modeling has culminated in our convener's MULTI program (Carlsson, 1986); it is habitually used worldwide to calibrate reliably how photons encode physical information from stellar photospheres. The unambiguous identification of the solar  $p$  modes came from the comparison between Deubner's (1975) observed  $(k, \omega)$  ridges and the  $(k, \omega)$  resonance loci in the detailed numerical Ando and Osaki (1975) quantification of Ulrich's (1970) subsurface cavities; the agreement was "embarrassingly" good (Deubner, 1975) and founded helioseismology. Granulation studies went from morphology to physical insight when Nordlund (1982) pioneered time-dependent 3D simulation; solar granulation is now by and large understood (Spruit *et al.*, 1990) and stellar granulation predicted (Nordlund

and Dravins, 1990).

At present, a similar topic of promising confrontation between detailed observed properties and detailed numerical simulation consists of the so-called three minute oscillation of the so-called internetwork chromosphere. The primary observed properties include the spectral development of the so-called  $K_{2V}$  grains and the Fourier signatures, especially phase relationships, along radial lines of sight into the atmosphere; these are in principle well modelable by one-dimensional simulations. The current Oslo  $K_{2V}$  grain simulations deliver “embarrassingly good” reproduction of observed spectral behaviour; they permit insights into the physics of grain formation as extolled elsewhere in these proceedings. More lofty quests are to obtain reliable heating and cooling budgets, the overall energy balance, and the identification of the so-called basal flux.

This review emphasizes the observational side of this subject. It cannot be comprehensive; rather, in the spirit of our meeting, I flavour the topic with some of my own prejudices. The older literature has been covered in the extensive review by Rutten and Uitenbroek (1991a); it is good to note that there is much new work along lines then marked as prospective, settling issues left open at the time.

## 2. Context

Figure 1 displays chromospheric context in ESA viewgraph style. It shows that things really differ when one goes up from the photosphere, and it concludes by advertising space because it was made for an ESA planning workshop (Rutten, 1993). Indeed, when going up from the photosphere the ultraviolet is eventually needed for nearly any problem; it is fair to say, especially here in Oslo in view of the strong ITA commitment to ultraviolet spectrometry, that the future of much chromospheric physics rides on SOHO.

<i>Regime A</i>	<i>Regime B</i>
PHOTOSPHERE	UPPER ATMOSPHERE
<ul style="list-style-type: none"> <li>• radiation</li> <li>• hydrodynamics</li> <li>• doesn't feel higher layers</li> <li>• characteristic scales:               <ul style="list-style-type: none"> <li>– photon mean free path</li> <li>– pressure scale height</li> </ul>               10 – 100 km             </li> <li>• thick</li> <li>• success stories</li> <li>• visible</li> <li>• ground</li> </ul>	<ul style="list-style-type: none"> <li>• MHD</li> <li>• plasma physics</li> <li>• subject to photosphere</li> <li>• characteristic scales:               <ul style="list-style-type: none"> <li>– Alfvén resonance</li> <li>– current dissipation</li> </ul>               0.1 – 10 km             </li> <li>• thin</li> <li>• lots to do</li> <li>• ultraviolet &amp; X-ray</li> <li>• space</li> </ul>

Fig. 1. Two solar regimes.

The chromospheric dynamics discussed in this workshop, however, is largely limited to radiation hydrodynamics, rather than MHD and plasma physics, and is studied primarily with Ca II H & K, with a remarkable convergence to these lines from the Ca II infrared triplet in Würzburg (Deubner *et al.*, 1994), from H $\alpha$  in Göttingen (Kulaczewski, 1992; Kneer and von Uexküll, 1993), from the infrared and ultraviolet in Paris (Bocchialini *et al.*, 1994), and from the wings in Boulder (Lites *et al.*, 1993). Likewise, numerical duplication of the observed Ca II H & K phenomena constitutes an actively sought goal, with an equally remarkable convergence between various theoretical groups (Rammacher and Ulmschneider, 1992; Sutmann and Ulmschneider 1994a, 1994b; Fleck and Schmitz 1991, 1993; Kalkofen *et al.*, 1994; Carlsson and Stein, 1992; Carlsson, these proceedings) that have diverged from earlier collaborations (Klein *et al.* 1976, 1978; Schmitz *et al.*, 1985). All these ongoing studies aim at understanding H $_2V$  & K $_2V$  grains as part of the chromospheric three-minute oscillation in the quiet-Sun internetwork regime. Let me discuss these terms one by one.

Ca II H $_2V$  & K $_2V$  grains were first described by Hale and Ellerman (1904) as “minute bright calcium flocculi”, a better name than “grains” or “points”. They stand out on Gillespie’s often-published image (Skumanich *et al.*, 1984; Lites, 1985a, 1985b; Gaizauskas, 1985; Zirin, 1988; Rutten and Uitenbroek 1991a, 1991b; Skartlien, 1994)<sup>1</sup> as fairly roundish features, in contrast to the more elongated streaks marking the network. However, perhaps they stand out a bit too sharp in this image due to a fortuitous combination of exposure and photographic gamma in addition to the excellent seeing. Using the IDL ADJCT command to play with a digital K $_2V$  image teaches one quickly that changing gamma and clipping boundaries changes the appearance appreciably; grains are then seen to be brightness maxima in a larger-scale oscillation pattern. To quote Cram and Damé (1983):

“At many positions, both inside and outside the network, the H index [the intensity in a 1 Å passband around H $_3$ ] shows repetitive intensity variations with periods in the range 3–5 minutes. The apparent spatial scale of this oscillation is larger than that of the brightest cell points. This fact may be verified most readily by concentrating on the dark oscillating elements, which presumably correspond to the “dark clouds” discussed by Bappu and Sivaraman (1971) and Zirin (1974). Despite the disparity between the apparent scales of the oscillating elements and the bright cell points, the two phenomena are intimately connected, since the cell points invariably appear as localized intensity maxima in the more diffuse brightness maxima of the oscillation.”

Thus, K $_2V$  grains stick out as iceberg tops to show oscillation maxima, perhaps nonlinearly enhanced. On single filtergrams, they are not readily distinct from the grains in the calcium network or from internetwork *persistent flashers* (Brandt *et al.* 1992, 1994). Thus, K $_2V$  grains do not form a sharply defined class; a better definition is perhaps to designate as “K $_2V$  grains” those bright H $_2V$  and K $_2V$  features that belong to the pattern best seen in the time-resolved spectrograms in Fig. 4 of Cram and Damé (1983) and cartoonized in Fig. 2 of Rutten and Uitenbroek (1991a): small, short lived, narrow-band violet-side emission peaks at the moment of large K $_3$  dip redshift, preceded by contracting dark wing whiskers and gradually increasing K $_3$

---

<sup>1</sup> notwithstanding differences in cropping, orientation and sign, these are all part of a single McMath K $_2V$  spectroheliogram. Presumably Bill Livingston prints yet another piece of it whenever somebody asks for a high-resolution calcium image. Bruce Gillespie is now site manager of the Apache Point Observatory and happily surprised by the longevity of his plate.

redshift, and followed by wing darkness and a rapid  $K_3$  maneuver to the blue.

The *chromospheric three-minute oscillation* is sometimes supposed to be an oscillation exclusive to the chromosphere and exclusively at three minute periodicity. It isn't. Rather, it is the upward (in frequency  $f$ ) extension of the band of  $p$ -mode acoustic power across the cutoff frequency<sup>2</sup>, covering about 4–8 mHz or signals with 2–4 min periodicity. In velocity signals it gains dominance over the photospheric five-minute band around  $f = 3.33$  mHz when one goes up in the atmosphere, as already shown by Evans *et al.* (1963) and Noyes and Leighton (1963), and most vividly demonstrated in Fig. 1 of Noyes (1967), on the cover of GONG1992 (Brown, 1993, taken from Harvey *et al.*, 1993), and in Fig. 1 of Cram (1978). The latter paper represents a direct Fourier counterpart to the space-time presentations of Cram and Damé (1983) but is scandalously underquoted; its concise displays of power spectra for and coherency and phase difference between many diagnostics outdo much of the subsequent literature on chromospheric oscillations. The first column of its Fig. 1 shows a blob of power which steadily progresses to higher frequency in the Ni I 5894 Å—Na I D<sub>2</sub>—Ca II 8542 Å—H $\alpha$ —K<sub>3</sub> sequence, reaching a wide spread in  $f$  for K<sub>3</sub>. In the corresponding intensity column, a similar blob follows (at a definite lag in Na I D<sub>2</sub>, demonstrating that its Doppler shift responds to higher layers than its brightness) up to Ca II 8542 Å, but vanishes for H $\alpha$  and K<sub>3</sub>. This difference shows that something drastic happens between photosphere-sensitive lines as Ca II 8542 Å and truly chromospheric lines as Ca II K<sub>3</sub>, making it unlikely that the three-minute oscillation is simply a propagating extension of the regular evanescent five-minute waves below the cutoff frequency.

On the other hand, recent work<sup>3</sup> indicates modal structure in the three-minute regime similar to the familiar  $p$ -mode parabolae in diagnostic diagrams<sup>4</sup> (*e.g.*, Libbrecht, 1988; Duvall *et al.*, 1991; Fernandes *et al.*, 1992; Kneer and von Uexküll, 1993; Deubner *et al.*, 1994; Fleck, these proceedings), extending well above the cutoff frequency even at large wavenumbers—also in Fernandes *et al.* (1992) although these authors claim otherwise<sup>5</sup>.

These high-frequency ridges seem direct continuations of the  $p$ -mode ones, but have discontinuities in their properties at the cutoff frequency. Kumar explains them as pseudomodes, not due to a chromospheric cavity—for example one bounded by the transition region as proposed by Mein and Mein (1976) and more recently by Balmforth and Gough (1990), or a cavity bounded by an isothermal layer as proposed by Narasimha (1993)—nor as direct extensions of the  $p$ -mode ridges, but rather due to interference between waves that propagate directly up from a subsurface source and waves that are reflected only once at subsurface layers (Kumar and Lu, 1991; Kumar, 1993; Kumar, 1994; Kumar *et al.*, 1994). The time–distance representation of Duvall *et al.* (1993b) agrees with this interpretation since their high-frequency diagram shows only a single reflection locus. This result does not directly imply that

<sup>2</sup> with  $f_{AC} = 5.55$  mHz or  $P_{AC} = 3.00$  min for long wavelengths according to Fossat *et al.* (1992); at higher wavenumber  $f_{AC} \approx k_h$  in the usual units of mHz and rad Mm<sup>-1</sup>.

<sup>3</sup> I wonder whether high- $f$  ridges weren't already discernible in Fig. 2 of Mein and Mein (1976).

<sup>4</sup> The axes of the classical  $(k, \omega)$  diagram should be replaced by frequency  $f$  and degree  $l$ , in order to do away with awkward factors  $2\pi$  and to make it the  $f - l$  diagram or FLD in honour of Franz-Ludwig Deubner.

<sup>5</sup> Perhaps due to a factor  $2\pi$ ?

the high- $f$  sources are localized, since the technique assumes point sources and annular receivers only in a mathematical sense. Other work, however, indicates that in general the excitation of the solar  $p$ -mode occurs in quite localized sources that are only about 50–100 km below the surface (Brown, 1991; Goode *et al.*, 1992; Duvall *et al.*, 1993a; Kumar, 1994). The concept leads to current efforts in “local” helioseismology, using localized flux vector analysis, time-distance analysis or 3D Fourier trumpet and ring analysis to measure subsurface source properties and horizontal flows tomographically (Braun *et al.*, 1992; Korzennik *et al.*, 1995; Hill, 1995; Hill *et al.*, 1995). The ridges extend out to high frequency and to fairly high spatial wavenumbers for photospheric lines, less so for  $K_3$  brightness (Deubner *et al.*, 1994). Harvey *et al.* (1993) fit an appreciable power background under the ridges in a wide-band low-resolution long-duration CaII K intensity power spectrum.

The next term to discuss is *internetwork*. This term was preferred by Lites *et al.* (1993) over *inner network* (used by Livingston and Harvey), *intranetwork* (Martin, Zirin) or *cell interior* (Deubner and Fleck, Kneer and von Uexküll) on the basis of an experiment by Karel Schrijver. He handed the same magnetogram to various Utrecht colleagues with the request to draw network cells by eye. I was in a hurry and discerned only a few; Kees Zwaan meticulously outlined a large number at various scales; others drew others. The non-uniqueness demonstrated that the magnetic network (and so the calcium network) does not outline regular cellular mosaics as the supergranulation perhaps does. Instead, it consists of crinkled segments in irregular patterns without well-defined insides, and is actually well described by percolation theory (Schrijver *et al.*, 1992; Balke *et al.*, 1993; Lawrence and Schrijver, 1993; Schrijver, 1994). Thus, *internetwork* defines small areas of quiet Sun without network; Keller *et al.* (1994) propose *non-network*.

In the chromosphere, the three-minute oscillation is primarily an internetwork phenomenon. This is already known since Liu and Sheeley (1971) whose analog Fourier analysis consisted of placing a photocell behind a small hole in the screen on which they projected movies of  $K_{2V}$  spectroheliograms. A digital remake in Fig. 4 of Lites *et al.* (1993) illustrates that network elements do not share in the three-minute oscillation but fluctuate with 5–20 min periodicities.

Other internetwork phenomena are the 160 nm *bright points* (Foyng and Bonnet 1984a, 1984b) and *CI jets* (Dere *et al.* 1983, 1986) which may or may not be directly related to  $K_{2V}$  grains; they are addressed by Hoekzema elsewhere in these proceedings. The same holds for the chillingly cool CO *clouds* (*e.g.*, Ayres 1981, 1991), necessarily an internetwork phenomenon if they exist. They are addressed by Uitenbroek elsewhere in these proceedings.

The nature of *internetwork magnetic fields* is even less certain. At sufficient sensitivity and spatial resolution, magnetic flux seems present in patches of a few seconds of arc in pepper-and-salt mixed-polarity patterns throughout internetwork areas (Livingston and Harvey, 1971). Keller *et al.* (1994) find that the intrinsic field strength is below one kG. Whether and how these internetwork fields interact with the internetwork three-minute oscillation, especially the  $K_{2V}$  grains, remains a matter of debate. Sivaraman maintains his claim of one-to-one correspondence between  $K_{2V}$  grain intensity and field strength (Sivaraman and Livingston, 1982; Sivaraman, 1991; Kariyappa *et al.*, 1994). Others believe  $K_{2V}$  grains to be purely

hydrodynamical (Rutten and Uitenbroek 1991a, 1991b; Deubner, 1991; Kulaczewski, 1992; Kneer and von Uexküll, 1993) except when persistently migrating (Brandt *et al.* 1992, 1994), while Kalkofen has migrated from strong to weak to no field (Kalkofen 1989, 1991; Kalkofen *et al.*, 1992).

Finally, internetwork areas should be covered by *magnetic canopies*. So far, their role in internetwork dynamics has been limited to the suggestion of Deubner and Fleck (1990) that they collect mechanical energy from low-frequency juggling over wide areas and funnel this down into network elements as magneto-gravity waves. More is to be expected now that the attention of the prolificist<sup>6</sup> Sami Solanki rises from tubes to canopies (Solanki *et al.*, 1994a).

### 3. Characteristics of $H_{2V}$ and $K_{2V}$ grains

Let me now illustrate some of the above properties with representations from a two-hour spectrogram sequence obtained by B.W. Lites and me on October 15, 1991 at the NSO/Sacramento Peak Vacuum Tower Telescope. We registered a  $10 \text{ \AA}$  portion of the Ca II H line on one CCD, the He I 10830  $\text{\AA}$  region simultaneously on another. These spectrograms contain many lines and continuum or H-wing windows; fluctuation diagnostics have been measured for 46 different spectral features. Only a few are shown here, detailed analysis to be published more formally.

The main point of this section is that even the quiet internetwork atmosphere, so much easier to understand than the active fluxtube atmosphere, presents a dynamical mixture that needs to be disentangled in many dimensions and domains at the same time.

#### *Separation in bandwidth.*

Figure 2 shows the intensity in the Ca II H line for three spectral bandwidths in the form of space-time images (“time slices”). The righthand panel is the  $H_{2V}$  intensity; it contains network most noticeably around position 100 and regular  $H_{2V}$  grains especially to the right of that. The lefthand panel simulates the Mt. Wilson H & K photometer (Vaughan *et al.*, 1978); the  $1 \text{ \AA}$  wide H index in the middle panel simulates the spectroheliograph slit of Sivaraman and Livingston (1982). The three panels contain basically the same information. They differ primarily in the contrast and sharpness with which the grains and the network stand out. This similarity illustrates the above quote from Cram and Damé (1983): grains are small, narrow-band intensity spikes that belong to a larger-scale and wider-band oscillation pattern. The latter does not differ much between the three panels; only when comparing amplitudes, blinking, or measuring phase differences become differences between the panels apparent.

The figure shows that a very narrow bandwidth is not needed to study spatio-temporal patterns of chromospheric oscillations with Ca II K filtergrams. Indeed, on our  $0.3 \text{ \AA}$  FWHM La Palma movies (Brandt *et al.* 1992, 1994) bright  $K_{2V}$  grains are rare, but all internetwork areas show spidery brightness structures that seem to move and evolve at large ( $50\text{--}100 \text{ km s}^{-1}$ ) apparent phase speed, betraying wave

---

<sup>6</sup> most prolific publicist; see 1989–1993 A&A author index.

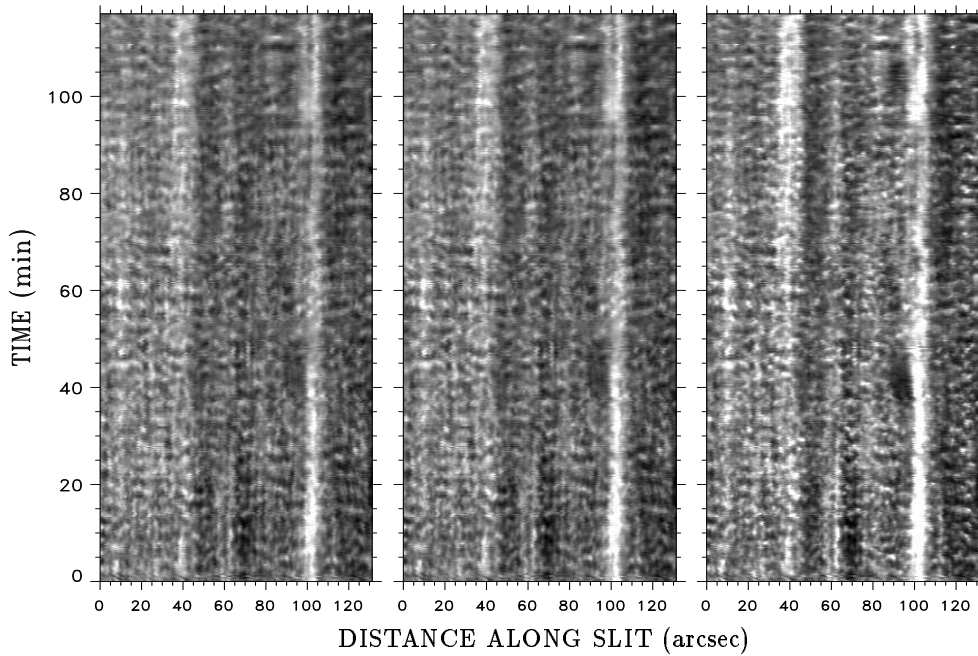


Fig. 2. Ca II H intensity behaviour as a function of spatial position along the slit. Left: measured with a centered triangular profile of 2 Å base, as the Mt. Wilson stellar H & K photometer. Middle: H index = intensity in a centered 1 Å wide band. Right:  $H_{2V}$  intensity.

interference. A narrow filter band is only required if one aims to measure the  $K_{2V}$  over  $K_{2R}$  intensity ratio as a filtergraph proxy for  $K_3$  Doppler shift (Rutten and Uitenbroek, 1991a; Lites *et al.*, 1994).

#### *Separation in height*

Figure 3 shows spatially resolved power spectra from the same data and is also discussed in Lites *et al.* (1994). The four lines sample the solar atmosphere in different fashions. The Fe I 3963.44 Å line (lower right panel) is the deepest-formed line in our data set because it is weak and furthest away from Ca II H line center. It shows granulation and/or gravity wave power at the lowest frequencies and contains the familiar  $p$ -mode band. The Al I 3961.54 Å resonance line (upper right panel) is quite strong and is probably rather like Ca II 8542 Å in its characteristics. Its higher formation results in a much larger contribution by the three-minute oscillation, but network/internetwork distinction is not yet clear. In contrast, Ca II  $H_3$  shows large distinction as usual. In this observation, contrary to the comparable plot in Fig. 4 of Lites *et al.* (1993), there is appreciable three-minute power only at the far right, corresponding to frequent occurrence of  $H_{2V}$  grains only at the far right in the  $H_{2V}$  panel of Fig. 2.

He I 10830 Å (upper left) shows properties rather like  $H_3$ . This panel is very noisy due to the use of a non-optimized CCD camera and the weakness of the line, but generally, the He I power spectrum exhibits similar patterns as the Ca II panel.

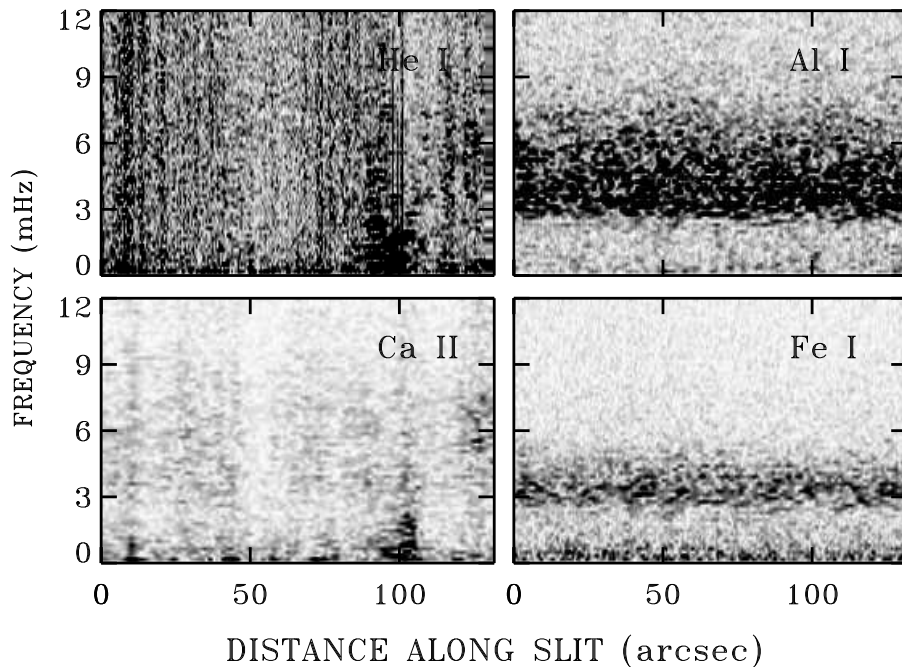


Fig. 3. Quiet-sun velocity power spectra from four lines that were registered simultaneously, respectively He I 10830 Å (upper left panel), Ca II H<sub>3</sub> (3968.5 Å, lower left), the strong Al I 3961.54 Å resonance line (upper right), and the weak Fe I 3963.44 Å line (lower right). The slit crossed network around position 100, as evident in Ca II. The square root of the Doppler shift power per position is coded as darkness. The striping at the far right in the He I panel is due to correction for differential refraction along the slit.

This agreement is illustrated by phase difference spectra in Lites *et al.* (1994). It is also seen in Figs. 2 and 3 (lower left and upper right panels, respectively) of Bocchialini *et al.* (1994) if one neglects the scaling and takes  $K_{2V} - K_{2R}$  as proxy for  $K_3$ , and also when one compares the He I 10830 Å – Mg I 8807 Å phase difference spectrum in Fig. 3 of Fleck *et al.* (1994) with the upper-left panel of Fig. 5 below. Note, however, that the agreement is qualitative; the He I rms velocity amplitude is appreciably smaller than for H<sub>3</sub>.

Such comparisons between different lines are the major contribution that spectrometry makes to studies of chromospheric dynamics. They also provide the major testing ground for the numerical simulations, all one-dimensional so far and emulating fixed-slit spectrometry. The simulations imply that at the height of Ca II H & K line formation, the three-minute oscillation consists of overtaking shock trains far out of the linear regime, with much temporal (and presumably spatial) interference (see references above and reports elsewhere in these proceedings). This implies that classical concepts of plane-parallel line formation, with lines regularly ordered in

well-behaved “height of formation”, make no sense. The early work of Mein (1964, 1966, 1971) and coworkers (Mein and Mein, 1976, 1980; Provost and Mein, 1979) showed that even the response of the CaII infrared lines to quasi-linear waves is already quite complex, especially that of CaII 8498 Å. Now that we have to do with interfering shocks rather than with clean waves, interpretation of observed spectral line differences, in particular phase difference spectra, must necessarily rely on numerical simulation.

It seems to me that this holds self-evidently for the lefthand panels of Fig. 3. The amazing agreement between CaII and HeI Doppler shifts says that the two lines experience the same phenomenon in roughly similar fashion, notwithstanding their large difference in formation sensitivities. The latter may produce the difference in amplitude, not in the sense that “He I 10830 Å is formed higher and therefore its smaller rms Doppler shifts imply that the oscillation has smaller amplitude at greater height”, but rather that the formation of the He I line weighs the excursions along the line of sight in the layers where coalescing shocks and downfalling after-shock matter interact somewhat differently from CaII H, no wonder since it combines smaller opacity with a very different temperature and irradiation sensitivity. Thus, the localization of the line response is primarily done by the actual dynamical stratification, not by the average line contribution function. A similar issue holds for the CI jets discussed by Hoekzema in these proceedings. Their observed Doppler shifts are up to  $20 \text{ km s}^{-1}$ , very much larger than the  $K_3$  shifts, but nevertheless seem to belong also to the internetwork three-minute dynamics.

#### *Separation in frequency*

In separating time-sequence data frequency-wise by Fourier transforms one loses the identification of space-time behaviour. This is not permitted when different areas behave differently; a major difference between the Fourier analysis of Cram (1978) and the subsequent studies of Lites *et al.* (1982), Deubner and Fleck (1990), Kulaczewski (1992), Lites *et al.* (1993), Kneer and von Uexküll (1993) and Bocchialini *et al.* (1994) is that the latter all distinguish network from internetwork areas.

The alternative to plotting Fourier diagnostics with area distinction is to plot space-time diagnostics with Fourier distinction; this is done in Fig. 4. The input consists of the  $H_{2V}$  brightness time slice shown in the upper-left panel, the same as the right-hand panel in Fig. 2. The three lower panels show its Fourier constituents in terms of the major three phenomena present in the internetwork chromosphere: the low-frequency gravity wave band, the five-minute  $p$ -mode band, and the three-minute propagating wave band. They were made by filtering the signal per spatial column with appropriate passbands in temporal frequency. We have split all our 46 spectral diagnostics in these three bands. It is instructive to blink these 138 Fourier-filtered time slices in varied combinations and to study *e.g.*, the reversal of granular intensity in the outer H-line wings (Evans and Catalano, 1972; Suemoto *et al.* 1987, 1990; cf. Salucci *et al.*, 1994) and the spatio-temporal relationships between large-amplitude oscillation wave trains at different heights. Such blinking is not useful for the unfiltered time slices in which the three constituents confuse each other thoroughly.

The difference in character between the leftmost lower panel and the other two

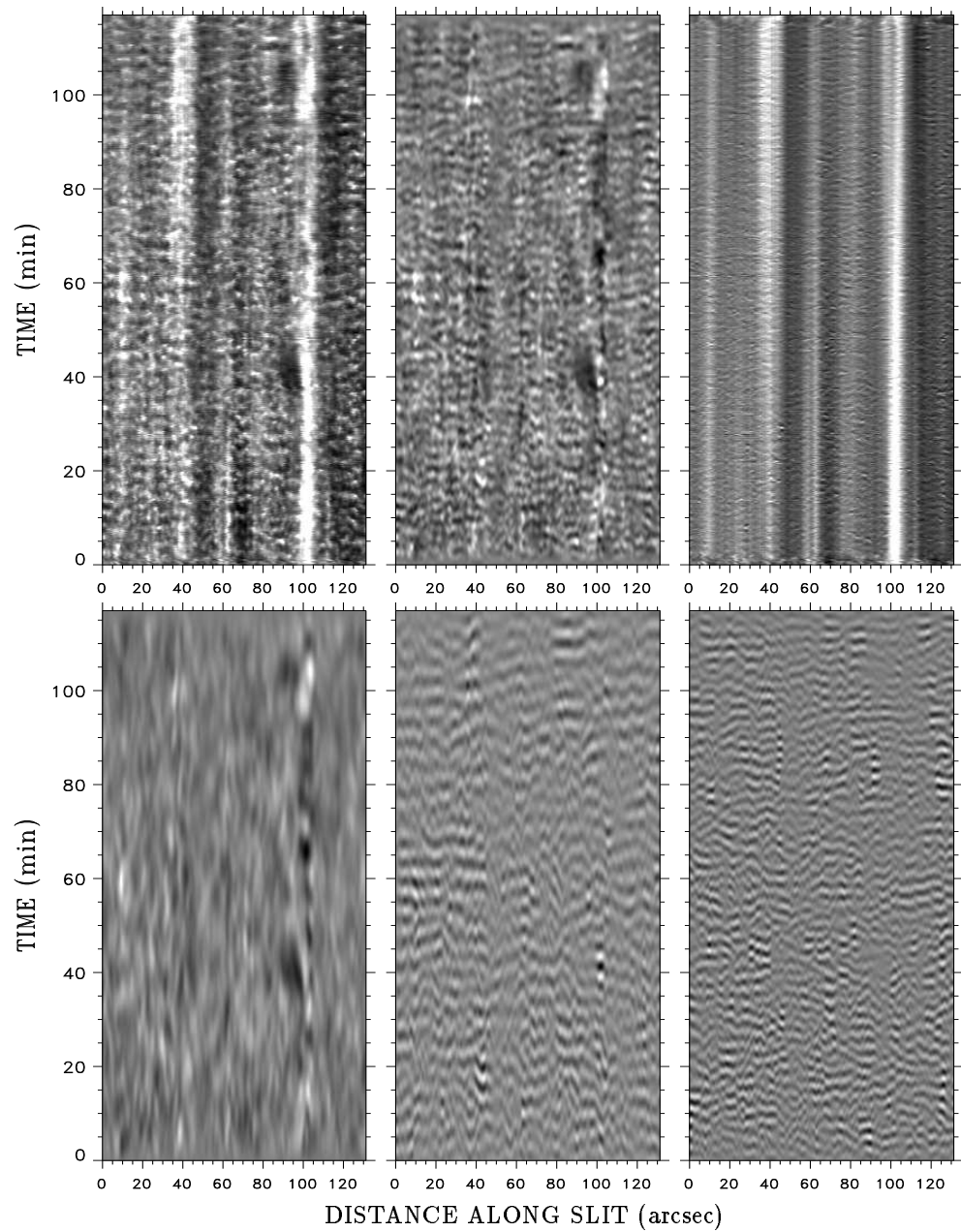


Fig. 4. Space-time Fourier decomposition. Each panel is a time slice plotting  $H_{2V}$  intensity as a function of spatial position along the slit and elapsed time. The upper left panel contains the measurements. The lower three panels, from left to right, are the low- $f$  band, five-minute band and three-minute band components. The sum of the lower three panels is shown in the upper middle panel. It displays total oscillatory behavior. The upper right panel is the difference between the first and second panels and displays only the lowest and highest frequencies. The grey scale has been set by clipping the  $H_{2V}$  intensity at a bright network value.

lower panels is immediately apparent. The first panel is space-time structured by granular overshoot and granulation-excited gravity waves. The network stands out clearly with its own slow fluctuations. The other two panels are very similar in character, showing typical wave pattern interference with supersonic apparent phase speeds (the tilts of the wavy-curtain modulation)<sup>7</sup>. The network around position 100 tends to have larger five-minute and smaller three-minute amplitude. It possesses oscillation maxima in the five-minute band, whereas the H<sub>2V</sub> grains to the right of it have high-amplitude three-minute components.

The middle panel in the upper row of Fig. 4 is the sum of the lower three and displays oscillation characteristics with normalization per column (low frequencies taken out) and less noise (high frequencies out)<sup>8</sup>. This panel shows the slow network modulation most clearly. It gives a strong impression of regular periodicity, as reported for older data by Lites *et al.* (1993).

#### *Separation in context*

The upper left and right panels in Fig. 4 display most clearly that the slit cuts through different chromospheric regimes. Network stands out around position 100 and is also present around position 40. The area around 120 arcsec is internetwork with many H<sub>2V</sub> grains, whereas there is a dark internetwork area without grains at 50 arcsec. Finally, the stripe near 10 arcsec is very much like the persistent flasher traced by Brandt *et al.* (1992) on a K<sub>2V</sub> filtergram sequence and shown by Brandt *et al.* (1994) to be an actual solar cork, obeying the horizontal flows in the underlying photosphere and therefore presumably magnetically anchored. The upper part of the strip would not be easily recognized as such, but the lower part is very much similar to the track in Fig. 2 of Brandt *et al.* (1992). That flasher migrated fairly rapidly through the internetwork area; this one has fortunately stayed on the spectrograph slit.

Thus, it appears that splitting the quiet chromosphere into network and internetwork regimes alone does not pay sufficient tribute to actual solar variation. Summing over large areas and long times may produce statistical stability and clean diagrams, but also implies averaging over signals that may differ intrinsically. The reverse is therefore done in Fig. 5, where the display technique of the phase difference spectra in Lites *et al.* (1993), designed to show spread in addition to averaged result, is carried a step further by limiting the phase determinations to small spatial areas, *i.e.*, the narrow strips just noted. The scatter increases, but so may the actual solar information content<sup>9</sup>.

The diagrams in Fig. 5 are for AlI 3961.54 Å and H<sub>3</sub> Dopplershift, upward velocity positive and phase difference positive when AlI shift leads H<sub>3</sub> shift. The four AlI power spectra are similar but the H<sub>3</sub> power spectra differ with location along the

<sup>7</sup> Note that such filtering may lead to apparent over-regularity. A short segment of large amplitude forces its phase on the remainder of its time-slice column if the filter passband is too narrow (cf. Damé and Martić, 1987; Martić and Damé, 1989).

<sup>8</sup> Such filtering would have improved the time slices in Fig. 2 of Kneer and von Uexküll (1993) which are badly fringed at twice the Nyquist frequency.

<sup>9</sup> In any case, the displayed information content of these "Bruce Lites confusograms" is increased by adding frequency-averaged phase differences, rms error bars, coherency and power spectra all into a single panel.

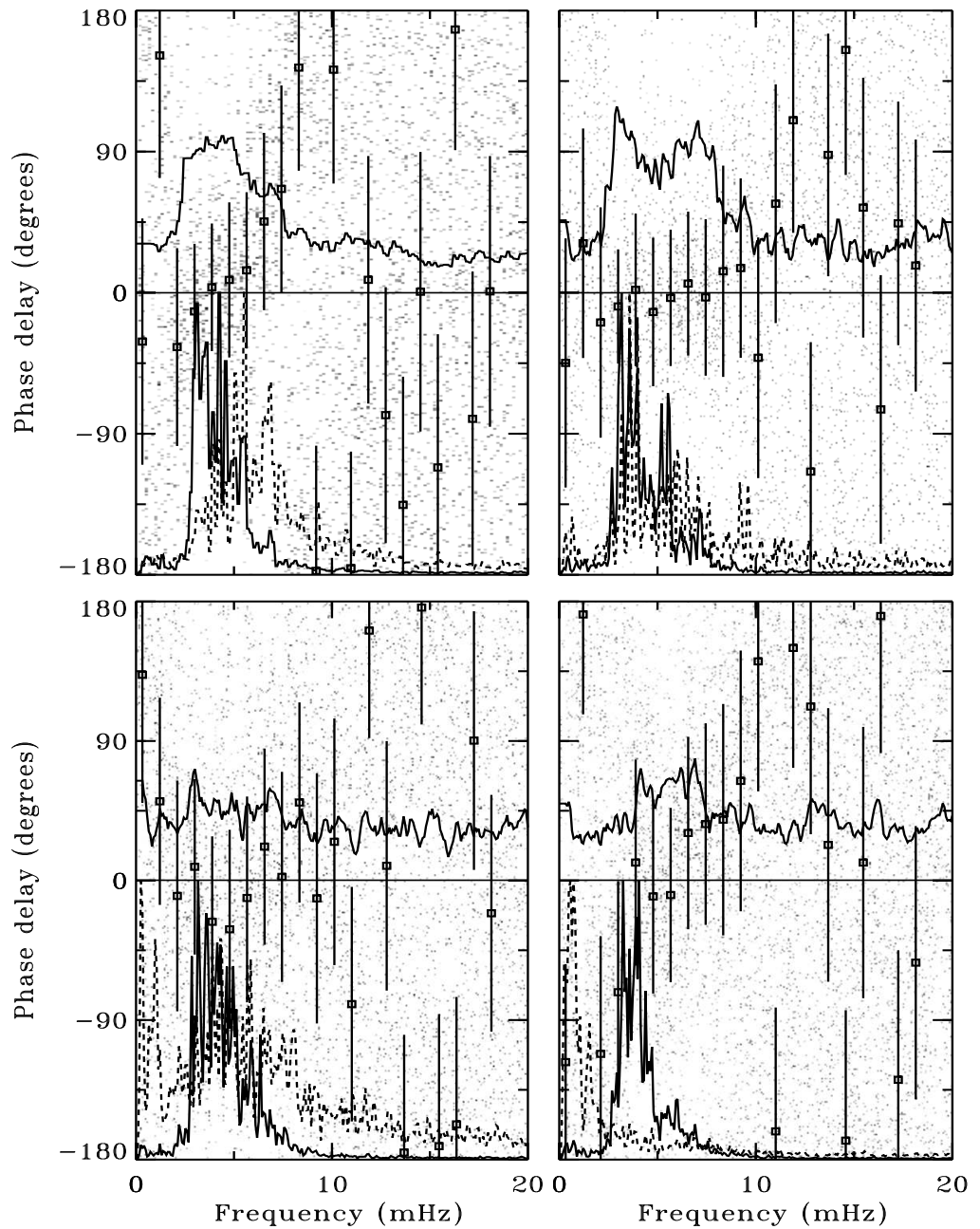


Fig. 5. Phase difference spectra between AlI 3961.54 Å and CaII H<sub>3</sub> Doppler shifts, computed following Lites *et al.* (1993). In each panel, the grey-scaled dots mark amplitude-weighted phase difference per frequency bin and per spatial position along the slit. The squares mark their average per frequency bin, the bars the corresponding rms deviations. The curve in the upper half is the coherency, scaled 0–1 and determined by 9-point smoothing in temporal frequency. The curves in the lower half are the power spectra, solid for AlI 3961.54 Å and dashed for H<sub>3</sub>, each normalized by its maximum. Upper left panel: area restricted to positions 116–131 arcsec along the slit, with many H<sub>2V</sub> grains as seen in Figs. 2 and 4. Upper right panel: area at 6–15 arcsec with persistent flasher. Lower left panel: dark area at 46–57 arcsec. Lower right panel: network area at 93–106 arcsec.

slit, as is also seen in Fig. 3. The upper-left diagram is for the  $H_{2V}$  grain strip near position 120. It is the only one with most  $H_3$  power above  $f = 5$  mHz. It has fairly high coherence and shows a steady increase of phase difference with frequency throughout the three-minute band, turning into noise above  $f = 10$  mHz. The persistent flasher (upper right diagram) has similar coherence but its  $H_3$  power peaks at five minutes and its phase differences remain close to zero throughout the region of coherence. The dark area (lower left diagram) has no coherence, low  $H_3$  power<sup>10</sup> and noisy phase differences that scatter around zero. Finally, the network diagram at the lower right displays familiar network behaviour: it has strong  $H_3$  power at very low frequencies and an increase of phase difference with  $f$  in the three-minute regime.

Clearly, a larger data set is desirable to decrease the  $1\sigma$  error bars in these diagrams. Even so, it seems unwise to average persistent flashers and dark areas together with grainy areas into one “internetwork” bin. These diagrams indicate that flashers and dark areas pull the three-minute phase differences to zero. The  $H_{2V}$  grain panel shows an increase from  $0^\circ$  to  $140^\circ$  over  $f = 5 - 8$  mHz which is just like the simulated increase in Fig. 49 of Skartlien (1994) after reversal for sign convention.

The phase difference plots measure oscillation characteristics from all pixels in the selected time-slice strip. What about the  $K_{2V}$  grain pixels specifically? Since grains are part of the larger-scale three-minute oscillation they should obey these phase differences. A direct display is given in Fig. 6 in the form of scatter plots. These correlate the measured  $H_{2V}$  intensity per spatial position in the  $H_{2V}$  grain strip (positions 116–131 arcsec) to the three-minute components of the AII 3961.54 Å Doppler shift (left) and the intensity in an H-line wing window (right), *i.e.*, the values in the two Fourier-decomposed three-minute time slices of these quantities are simply plotted against each other per pixel in the grain strip. The plots are a statistical extension of the case studies of *e.g.*, Jensen and Orrall (1963), Punetha (1974), Liu (1974), Beckers and Artzner (1974), Cram (1974), Durrant *et al.* (1976) and Cram *et al.* (1977). The upper panels show a cloud of points with an upward extension, the latter points being from the high-intensity  $H_{2V}$  grains. In the middle and lower panels, a time delay was introduced between the AII 3961.54 Å and H-wing sampling and the  $H_{2V}$  sampling, of one and two minutes respectively. The tilting of the clouds betrays two-minute periodicity. The  $H_{2V}$  grains concur with it; thus, bright grains correlate with the oscillation underneath the  $H_{2V}$  formation layer after some delay.

The lefthand diagrams correspond to phase difference analysis between AII shift and  $H_{2V}$  brightness while the righthand diagrams correspond to  $I - I$  phase differences, but these diagrams distinguish, at the cost of frequency resolution, between the phase-difference contributions of bright, average and dark  $H_{2V}$  pixels. There is no symmetry between bright and dark; the clouds do not have co-oscillating dark extensions. Whenever  $H_{2V}$  shows enhanced brightness, AII 3961.54 Å blueshift was large two minutes earlier; however, the reverse does not hold since large AII

---

<sup>10</sup> Perhaps one ought to normalize the power spectra to their high- $f$  noise level. Bocchialini *et al.* (1994) regard differences between high- $f$  power tails as significant, but I would rather attribute these to difference in small-scale morphology that is jittered by seeing across the slit.

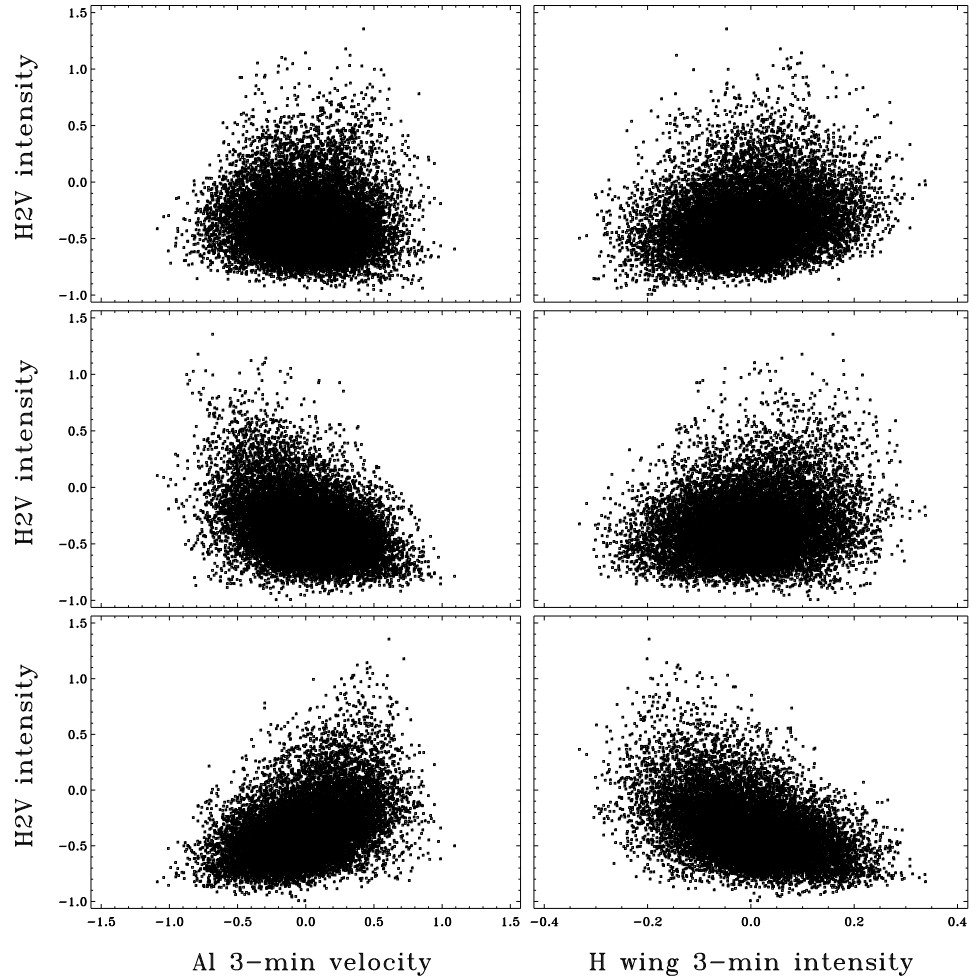


Fig. 6.  $H_{2V}$  intensity against the three-minute bands of respectively AlI 3961.54 Å Doppler shift (left) and H-line wing brightness near 3967.74 Å (right), per slit position of the grain-rich data segment at the far right of the  $H_{2V}$  time slice in Figs. 2 and 4. Top: simultaneous sampling. Middle: abscissae measured one minute before  $H_{2V}$  intensity. Bottom: abscissae measured two minutes earlier. The AlI Doppler shift is in  $\text{km s}^{-1}$ , blueshift positive; the intensities are in arbitrary units with an arbitrary zero point.

3961.54 Å blueshift is more often followed two minutes later by average  $H_{2V}$ , and also often by dark  $H_{2V}$ . Also, the brightest  $H_{2V}$  points are not an extension of the cloud towards larger AlI 3961.54 Å shift or larger H-wing brightness. Another selector seems at work as well; Rutten and Uitenbroek (1991a) identified the downfall of higher layers as measured by  $H_3$  Dopplershift as a second requirement (their page 26) by overlaying the time slices in Cram and Damé (1983), a technique that is simulated in these scatter plots for the underlying atmosphere.

#### 4. Discussion

In their 1991 review, Rutten and Uitenbroek concluded that CaII H&K inter-network behaviour is primarily a hydrodynamical phenomenon in which the CaII wing whiskers portray regular upward propagating three-minute oscillations and the grains mark interference between these and a saw-tooth oscillation displayed by K<sub>3</sub> and consisting either of nonlinear waves, 2–3 min shock trains, or modulation of high-frequency shock trains. Rather than calling the grains tops of icebergs, they compared them to the water spouts seen at sea in places with much wave pattern interference, designated *clapotis* on sea charts (Dowd, 1981<sup>11</sup>).

The major change since then is that numerical modeling now converges to a definitive description of K<sub>2V</sub> grain formation. The earlier groundwork by *e.g.*, Stein and Schwartz (1972) and Leibacher *et al.* (1982) has blossomed into a flurry of numerical activity and hydrodynamical understanding. Ulmschneider's computations identified valuable concepts as the limiting shock strength (Ulmschneider 1990, 1992) and shock overtaking (Rammacher and Ulmschneider, 1992); Fleck and Schmitz (1991, 1993) clarified the basic physics of cut-off resonance, perhaps already clear to Lamb (1908) but not to us; the development now culminates here at Oslo with the proper inclusion of time-dependent radiation effects in the Carlsson–Stein code. The simulatory reproduction of the Lites *et al.* (1993) observations by Carlsson and Stein (1992) was already impressive; the results now in hand (see Carlsson's contribution in these proceedings) show unmistakably that the code produces K<sub>2V</sub> grains just like the solar ones. These simulations not only confirm early scenario's (Athay, 1970; Cram, 1972; Liu and Skumanich, 1974) and sophisticated empirical modeling by Mein *et al.* (1987), but add detailed physical insight by not being an ad-hoc scheme but a self-consistent application of reliable time-dependent hydrodynamics and radiative transfer, to be utilized to find out exactly how grains form at least in the computer. The grainy secret lies in having proper upper-layer dynamics at the right moment, not from the infalling meteorites postulated by Jewell (1900) but rather due to the intricacies of overtaking shock dynamics with time-dependent hydrogen ionization and recombination.

However, some issues remain. Obviously, one-dimensional simulations do not exactly assess the energy balance and the basal flux, or horizontal scales, piston patterning and wave interference. Let me conclude this review by discussing some of these.

##### *Spatial patterning*

Damé and Martić (1987) have claimed on the basis of the K<sub>3</sub> image sequence analyzed by Damé *et al.* (1984) that the K<sub>3</sub> brightness oscillation possesses a distinct, persistent horizontal wavelength of 8 Mm, similar to the one noted in 1600 Å continuum brightness variations (Foing and Bonnet, 1984a; Martić and Damé, 1989) and attributed by Deubner (1989) to *p*-mode interference patterns (*cf.* Straus *et al.*,

---

<sup>11</sup> A book your library doesn't have. A quote from the 1988 edition: "When the crests of such waves coincide, their amplitudes combine, creating huge standing waves, much steeper than traveling waves. This phenomenon is called *clapotis*. Off the northern tip of New Zealand, where major wave patterns collide in deep water, *clapotis* is regularly seen. The pinnacling waves formed here have so much vertical power that they can throw a laden kayak clear out of the water."

1992). It seems indeed that  $H_{2V}$  and  $K_{2V}$  grains cluster in meso-scale or larger-scale patterning. The “standard” grain development evident in Fig. 4 of Cram and Damé (1983) is actually rather rare; Carlsson and Stein (1992) had to hunt around in the data of Lites *et al.* (1993) to find a “typical” example. Kulaczewski (1992) found only sporadic, non-repetitive grains in his spectra. In the data presented above, grains are only frequent in the rightmost strip adjacent to the network (Figs. 2 and 4). Gillespie’s  $K_{2V}$  spectroheliogram indicates grain clustering within internetwork areas. The La Palma  $K_{2V}$  movie of Brandt *et al.* (1992) contains fairly extended internetwork areas without much grain activity.

Let me digress here for a moment to the patterning of photospheric oscillations. Figure 7 shows two power maps from Brown *et al.* (1992). The  $p$ -mode map shows the familiar weakening of five-minute oscillations in active regions (dark); the rest of the field displays  $p$ -mode interference modulation in rather homogeneous patterning except where magnetic field resides, just as one would expect for amplitudes that are set by global properties of the solar interior. The three-minute power map shows active region halos, also described by Braun *et al.* (1992); the quiet regions have largest 3-min power in small-scale blobs that seem less homogeneously distributed than the  $p$ -mode blobs. There are fairly large areas of supergranular size without much power, while others abound with power blobs. Such spatial distribution seems to require another patterning agent than the pseudomode FLD ridges or the strong fields evident in the  $p$ -mode map. Brown *et al.* (1992) wonder whether these sites of excess high- $f$  emission sites are also the localized acoustic sources postulated by Brown (1991). In the  $K_{2V}$  grain context, the question arises whether excess  $K_{2V}$  graininess has to do with one or the other or both. The numerical simulations indicate that  $K_{2V}$  grains do not betray photospheric piston action in real time, since it takes many oscillation cycles before shock coalescence has set up the upper atmosphere into the proper state of turmoil for grains to flash in  $K_{2V}$ . A direct connection between large three-minute amplitude in the photosphere and grain activity is also not to be expected, nor seen in the data discussed above.

However, graininess patterning may yet betray piston activity statistically. Obvious granular piston candidates are the fast-sinking fingers of cool subsurface matter and the supersonic outflows near the borders or large granules that are consistently seen in granulation simulations (Stein and Nordlund, 1989; Cattaneo *et al.* 1989, 1990); the active region halos indicate there may also be magnetism-related ones (I would in particular suspect the persistent downdrafts adjacent to the flux sheets in the simulations of Steiner *et al.*, 1994). Granular pistoning may well be modulated on mesogranular scale, since regions of flow divergence tend to possess more exploding granules than converging ones (Title *et al.* 1989a, 1989b; Brandt *et al.*, 1991). Thus, it is of interest to correlate  $K_{2V}$  three-minute power maps as those of Damé *et al.* (1984) with deep magnetograms, with photospheric power maps as the ones of Brown *et al.* (1992), and with photospheric flow tracers, in each comparison admitting sizable delays between photospheric and  $K_{2V}$  patterning. Fortunately, the mesogranular evolution time of five to six hours (Brandt *et al.*, 1994) is longer than the half-hour delay between piston and upper-atmosphere grain state which the simulations indicate (Carlsson, these proceedings).

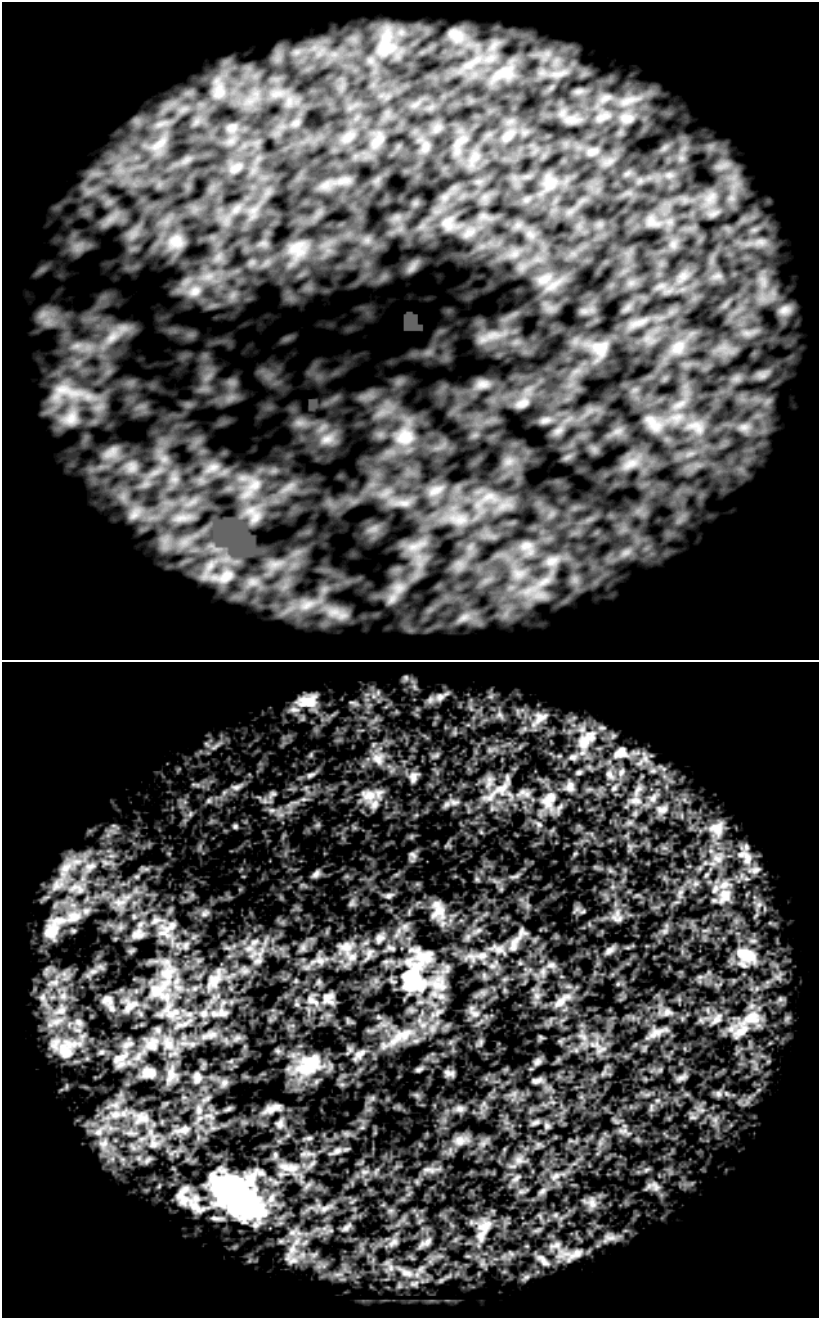


Fig. 7. Two oscillation power maps from Brown *et al.* (1992), constructed from a 256-min sequence of Fe I 5576 Å Dopplergrams. Top: power in the five-minute band. Dark areas correspond to active regions in a Kitt Peak magnetogram taken two hours earlier. Bottom: power in the three-minute band. The active regions have halos of enhanced power. The major axis measures 425 arcsec. The two brightest areas in the lower panel are artifacts and are masked in the upper panel. Both displays have been clipped to enhance contrast.

*Internetwork magnetism*

Although I have advocated that  $K_{2V}$  grains are a purely hydrodynamical phenomenon and that the grain-field correlation observed by Sivaraman and Livingston (1982) must be attributed to persistent flashers (Rutten and Uitenbroek, 1991a; Brandt *et al.*, 1992), the magnetic connection is not laid to rest until the Sivaraman-Livingston correlation is disproven by further (and better) observation—and actually, if internetwork fields are swept together or diluted by mesogranular convergent and divergent flows while these also pattern  $K_{2V}$  pistonning, a spatial correlation like the persistent mesogranular modulation of  $Mg\ I\ b_1$  noted by November (1989) is even likely. At the other end, higher up, the role of the magnetic canopies must be studied; they may figure directly in internetwork dynamics as speculated by Hoekzema elsewhere in these proceedings, and graininess differences may betray canopy differences. In brief, I still hold the hope expressed at the end of Rutten and Uitenbroek (1991a) that  $K_{2V}$  grains will sometime turn out useful to measure *something*.

*Internetwork chromosphere?*

A final comment is on nomenclature. The concept of a general BCA-HSRA-VALIII chromospheric temperature rise that sets in at a height of about 500 km in quiet-Sun internetwork regions is now being attacked from many sides. Avrett himself reproduces the multitude of strong CO lines observed from space by ATMOS with a model that decays gently out to large height ( $\log \tau_5 \approx -6$ ), much like a radiative equilibrium model. The recent CO observations of Uitenbroek *et al.* (1994) (see also Uitenbroek's contribution in these proceedings) indicate that cool CO clouds do not exist as permanent fixtures in the internetwork atmosphere since the CO lines are regularly modulated by oscillations, in a fashion closely comparable to the H & K wing modulation. Infrared eclipse and non-eclipse solar limb measurements indicate appreciable extent of a cool and dense component, presumably sitting above internetwork regions (Deming *et al.*, 1992; Solanki *et al.*, 1994b)—a trend which is continued at the larger heights seen in the sub-mm and mm regimes (Labrum *et al.*, 1978; Horne *et al.*, 1981; Wannier *et al.*, 1983; Lindsey *et al.*, 1986; Roellig *et al.*, 1991; Belkora *et al.*, 1992; Ewell *et al.*, 1993; White and Kundu, 1994) where the chromosphere is obviously not in hydrostatic equilibrium but perhaps not dominated by spicules either (cf. Ewell *et al.*, 1993), making one wonder whether the extended cool sub-mm and mm chromosphere is rooted in internetwork too. Last but not least, the numerical simulations shown in this workshop and the emulation of plane-parallel ultraviolet continuum modeling based on them, reported elsewhere in these proceedings by Carlsson and Skartlien, indicate that hot shock fronts embedded in a cool plasma may well masquerade as smooth outward temperature rise that does not exist as such anywhere.

All together, this implies that we need another name for the internetwork regime between  $h \approx 500$  km and  $h \approx 1500$  km. It is not part of the *photosphere* because it is transparent to the bulk of the solar flux. It is not part of the *chromosphere* when that is defined as the purple-red shell seen at eclipse because that sticks out much further; it is also not part of the chromosphere when that is defined as the regime above the VALIII temperature minimum because there is no such temperature minimum. I propose to call this regime of shocking wave interaction the *clapotisphere*.

**Acknowledgements.** I thank the Oslo Institute of Theoretical Astrophysics for inviting me to this miniworkshop. Various collaborations on chromospheric dynamics have been funded by NATO CRG travel grant nr. 900229 which is gratefully acknowledged. I am indebted to Tim Brown for Fig. 7 and to Bruce Lites who did the reduction of the 1991 data (other figures); I thank Bruce especially for his patience in waiting for me to describe the results. The NSO/Sacramento Peak staff assisting us with the observations consisted of Steve Hegwer, Richard Mann and Eric Stratton; Jo Bruls and Gianna Cauzzi helped with tape transfers.

## References

- Ando, H. and Osaki, Y.: 1975, *Publ. Astron. Soc. Japan* **27**, 581
- Athay, R. G.: 1970, *Solar Phys.* **11**, 347
- Ayres, T. R.: 1981, *Astrophys. J.* **244**, 1064
- Ayres, T. R.: 1991, in P. Ulmschneider, E. Priest, and B. Rosner (Eds.), *Mechanisms of Chromospheric and Coronal Heating*, Heidelberg Conference, Springer Verlag, Berlin, p. 228
- Balke, A. C., Schrijver, C. J., Zwaan, C., and Tarbell, T. D.: 1993, *Solar Phys.* **143**, 215
- Balmforth, N. J. and Gough, D. O.: 1990, *Astrophys. J.* **362**, 256
- Bappu, M. K. V. and Sivaraman, K. R.: 1971, *Solar Phys.* **17**, 316
- Beckers, J. M. and Artzner, G.: 1974, *Solar Phys.* **37**, 309
- Belkora, L., Hurford, G. J., Gary, D. E., and Woody, D. P.: 1992, *Astrophys. J.* **400**, 692
- Bocchialini, K., Vial, J.-C., and Koutchmy, S.: 1994, *Astrophys. J.* **423**, L67
- Brandt, P. N., Ferguson, S., Scharmer, G. B., Shine, R. A., Tarbell, T. D., Title, A. M., and Topka, K.: 1991, *Astron. Astrophys.* **241**, 219
- Brandt, P. N., Rutten, R. J., Shine, R. A., and Trujillo Bueno, J.: 1992, in M. S. Giampapa and J. A. Bookbinder (Eds.), *Cool Stars, Stellar Systems, and the Sun*, Proc. Seventh Cambridge Workshop, Astron. Soc. Pac. Conf. Series 26, p. 161
- Brandt, P. N., Rutten, R. J., Shine, R. A., and Trujillo Bueno, J.: 1994, in R. J. Rutten and C. J. Schrijver (Eds.), *Solar Surface Magnetism*, NATO ASI Series C433, Kluwer, Dordrecht, p. 251
- Braun, D. C., Lindsey, C., Fan, Y., and Jefferies, S. M.: 1992, *Astrophys. J.* **392**, 739
- Brown, T. M.: 1991, *Astrophys. J.* **371**, 396
- Brown, T. M. (Ed.): 1993, *GONG1992: Seismic Investigation of the Sun and Stars*, ASP Conference Series 42
- Brown, T. M., Bogdan, T. J., Lites, B. W., and Thomas, J. H.: 1992, *Astrophys. J.* **394**, L65
- Carlsson, M.: 1986, *A Computer Program for Solving Multi-Level Non-LTE Radiative Transfer Problems in Moving or Static Atmospheres*, Report No. 33, Uppsala Astronomical Observatory
- Carlsson, M. and Stein, R. F.: 1992, *ApJ Let* **397**, L59
- Cattaneo, F., Hurlburt, N., and Toomre, J.: 1990, *Astrophys. J.* **349**, L63
- Cattaneo, F., Hurlburt, N. E., and Toomre, J.: 1989, in R. J. Rutten and G. Severino (Eds.), *Solar and Stellar Granulation*, NATO ASI Series C-263, Kluwer, Dordrecht, p. 415
- Cram, L. E.: 1972, *Solar Phys.* **22**, 375
- Cram, L. E.: 1974, *Solar Phys.* **37**, 75
- Cram, L. E.: 1978, *Astron. Astrophys.* **70**, 345
- Cram, L. E., Brown, D. R., and Beckers, J. M.: 1977, *Astron. Astrophys.* **57**, 211
- Cram, L. E. and Damé, L.: 1983, *Astrophys. J.* **272**, 355
- Damé, L., Gouttebroze, P., and Malherbe, J.-M.: 1984, *Astron. Astrophys.* **130**, 331
- Damé, L. and Martić, M.: 1987, *Astrophys. J.* **314**, L15
- Deming, D., Jennings, D. E., McCabe, G., Noyes, R., Wiedemann, G., and Espenak, F.: 1992, *Astrophys. J.* **396**, L53
- Dere, K. P., Bartoe, J.-D. F., and Brueckner, G. E.: 1983, *Astrophys. J.* **267**, L65
- Dere, K. P., Bartoe, J.-D. F., and Brueckner, G. E.: 1986, *Astrophys. J.* **305**, 947
- Deubner, F.-L.: 1975, *Astron. Astrophys.* **44**, 371
- Deubner, F.-L.: 1989, *Astron. Astrophys.* **216**, 259
- Deubner, F.-L.: 1991, in P. Ulmschneider, E. Priest, and B. Rosner (Eds.), *Mechanisms of Chromospheric and Coronal Heating*, Heidelberg Conference, Springer Verlag, Berlin, p. 6
- Deubner, F.-L. and Fleck, B.: 1990, *Astron. Astrophys.* **228**, 506
- Deubner, F.-L., Hoffmann, J., Kossack, E., and Fleck, B.: 1994, in R. J. Rutten and C. J. Schrijver (Eds.), *Solar Surface Magnetism*, NATO ASI Series C433, Kluwer, Dordrecht, p. 155

- Dowd, J.: 1981, *Sea Kayaking*, University of Washington Press, Seattle
- Durrant, C. J., Grossmann-Doerth, U., and Kneer, F. J.: 1976, *Astron. Astrophys.* **51**, 95
- Duvall, T. L., Harvey, J. W., Jefferies, S. M., and Pomerantz, M. A.: 1991, *Astrophys. J.* **373**, 308
- Duvall, T. L., Jefferies, S. M., Harvey, J. W., Osaki, Y., and Pomerantz, M. A.: 1993a, *Astrophys. J.* **410**, 829
- Duvall, T. L., Jefferies, S. M., Harvey, J. W., and Pomerantz, M. A.: 1993b, *Nature* **362**, 430
- Evans, J. W. and Catalano, C. P.: 1972, *Solar Phys.* **27**, 299
- Evans, J. W., Michard, R., and Servajean, R.: 1963, *Ann d'Astrophys.* **26**, 368
- Ellwell, M. W., Zirin, H., Jensen, J. B., and Bastian, T. S.: 1993, *Astrophys. J.* **403**, 426
- Fernandes, D. N., Scherrer, P. H., Tarbell, T. D., and Title, A. M.: 1992, *Astrophys. J.* **392**, 736
- Fleck, B., Deubner, F.-L., Maier, D., and Schmidt, W.: 1994, in D. M. Rabin, J. T. Jefferies, and C. Lindsey (Eds.), *Infrared Solar Physics*, Proc. IAU Symp. 154, Kluwer, Dordrecht, p. 65
- Fleck, B. and Schmitz, F.: 1991, *Astron. Astrophys.* **250**, 235
- Fleck, B. and Schmitz, F.: 1993, *Astron. Astrophys.* **273**, 671
- Foing, B. and Bonnet, R. M.: 1984a, *Astron. Astrophys.* **136**, 133
- Foing, B. and Bonnet, R. M.: 1984b, *Astrophys. J.* **279**, 848
- Fossat, E., Régulo, C., Roca Cortés, T., Ehgamberdiev, S., Gelly, B., Grec, G., Khalikov, S., Khamitov, I., Lazrek, M., Pallé, P. L., and Sánchez Duarte, L.: 1992, *Astron. Astrophys.* **266**, 532
- Gaizauskas, V.: 1985, in B. W. Lites (Ed.), *Chromospheric Diagnostics and Modeling*, National Solar Observatory Summer Conference, Sacramento Peak Observatory, Sunspot, New Mexico, p. 25
- Goode, P. R., Gough, D., and Kosovichev, A.: 1992, *Astrophys. J.* **387**, 707
- Hale, G. E. and Ellerman, F.: 1904, *Astrophys. J.* **19**, 41
- Harvey, J. W., Jr., T. L. D., Jefferies, S. M., and Pomerantz, M. A.: 1993, in T. M. Brown (Ed.), *GONG1992: Seismic Investigation of the Sun and Stars*, Astron. Soc. Pac. Conf. Series, Vol. 42, p. 111
- Hill, F.: 1995, in R. K. Ulrich, E. J. Rhodes, and W. Däppen (Eds.), *GONG94: Helio- and Asteroseismology from Earth and Space*, ASP Conf. Series, in press
- Hill, F., Haber, D., Toomre, J., and Gough, D.: 1995, in R. K. Ulrich, E. J. Rhodes, and W. Däppen (Eds.), *GONG94: Helio- and Asteroseismology from Earth and Space*, ASP Conf. Series, in press
- Horne, K., Hurford, G. J., Zirin, H., and de Graauw, T.: 1981, *Astrophys. J.* **244**, 340
- Jensen, E. and Orrall, F. Q.: 1963, *Astrophys. J.* **138**, 252
- Jewell, L. E.: 1900, *Astrophys. J.* **11**, 234
- Kalkofen, W.: 1989, *Astrophys. J. Lett.* **346**, L37
- Kalkofen, W.: 1991, in P. Ulmschneider, E. Priest, and B. Rosner (Eds.), *Mechanisms of Chromospheric and Coronal Heating*, Heidelberg Conference, Springer Verlag, Berlin, p. 54
- Kalkofen, W., Rossi, P., Bodo, G., and Massaglia, M.: 1992, in M. S. Giampapa and J. A. Bookbinder (Eds.), *Seventh Cambridge Workshop on Cool Stars, Stellar Systems and the Sun*, Astron. Soc. Pac. Conf. Series, Vol. 26, p. 543
- Kalkofen, W., Rossi, P., Bodo, G., and Massaglia, S.: 1994, *Astron. Astrophys.* **284**, 976
- Kariyappa, R., Sivaraman, K. R., and Anadaram, M. N.: 1994, *Solar Phys.* **151**, 243
- Keller, C. U., Deubner, F.-L., Egger, U., Fleck, B., and Povel, H. P.: 1994, *Astron. Astrophys.* **286**, 626
- Klein, R. I., Stein, R. F., and Kalkofen, W.: 1976, *Astrophys. J.* **205**, 499
- Klein, R. I., Stein, R. F., and Kalkofen, W.: 1978, *Astrophys. J.* **220**, 1024
- Kneer, F. and von Uexküll, M.: 1993, *Astron. Astrophys.* **274**, 585
- Korzennik, S. G., Noyes, R. W., and Ziskin, V.: 1995, in R. K. Ulrich, E. J. Rhodes, and W. Däppen (Eds.), *GONG94: Helio- and Asteroseismology from Earth and Space*, ASP Conf. Series, in press
- Kulaczewski, J.: 1992, *Astron. Astrophys.* **261**, 602
- Kumar, P.: 1993, in T. M. Brown (Ed.), *GONG1992: Seismic Investigation of the Sun and Stars*, ASP Conf. Series 42, p. 15
- Kumar, P.: 1994, *Astrophys. J.* **428**, 827
- Kumar, P., Fardal, M. A., Jefferies, S. M., Duvall, T. L., Harvey, J. W., and Pomerantz, M. A.: 1994, *Astrophys. J.* in press
- Kumar, P. and Lu, E.: 1991, *Astrophys. J.* **375**, L35

- Labrum, N. R., Archer, J. W., and Smith, C. J.: 1978, *Solar Phys.* **59**, 331
- Lamb, H.: 1908, *Proc. London Math. Soc.* **7**, 122
- Lawrence, J. K. and Schrijver, C. J.: 1993, *Astrophys. J.* **411**, 402
- Leibacher, J., Gouttebroze, P., and Stein, R. F.: 1982, *Astrophys. J.* **258**, 393
- Libbrecht, K. G.: 1988, *Astrophys. J.* **334**, 510
- Lindsey, C., Becklin, E. E., Orrall, F. Q., Werner, M. W., Jefferies, J. T., and Gatley, I.: 1986, *Astrophys. J.* **308**, 448
- Lites, B. W. (Ed.): 1985a, *Chromospheric Diagnostics and Modeling*, Proceedings NSO Summer Conference, Sacramento Peak Observatory, Sunspot, New Mexico
- Lites, B. W.: 1985b, in H. U. Schmidt (Ed.), *Theoretical Problems in High Resolution Solar Physics*, MPA/LPARL Workshop, Max-Planck-Institut für Physik und Astrophysik MPA 212, München, p. 273
- Lites, B. W., Chipman, E. G., and White, O. R.: 1982, *Astrophys. J.* **253**, 367
- Lites, B. W., Rutten, R. J., and Kalkofen, W.: 1993, *Astrophys. J.* **414**, 345
- Lites, B. W., Rutten, R. J., and Thomas, J. H.: 1994, in R. J. Rutten and C. J. Schrijver (Eds.), *Solar Surface Magnetism*, NATO ASI Series C433, Kluwer, Dordrecht, p. 159
- Liu, S.-Y.: 1974, *Astrophys. J.* **189**, 359
- Liu, S. Y. and Sheeley, N. R.: 1971, *Solar Phys.* **20**, 282
- Liu, S.-Y. and Skumanich, A.: 1974, *Solar Phys.* **38**, 105
- Livingston, W. and Harvey, J.: 1971, in R. Howard (Ed.), *Solar Magnetic Fields*, IAU Symposium 43, Reidel, Dordrecht, p. 51
- Martić, M. and Damé, L.: 1989, in R. J. Rutten and G. Severino (Eds.), *Solar and Stellar Granulation*, NATO ASI Series C-263, Kluwer, Dordrecht, p. 207
- Mein, N. and Mein, P.: 1976, *Solar Phys.* **49**, 231
- Mein, N. and Mein, P.: 1980, *Astron. Astrophys.* **84**, 96
- Mein, P.: 1964, *Comptes Rendus* **258**, 819
- Mein, P.: 1966, *Ann. d'Astrophys.* **29**, 153
- Mein, P.: 1971, *Solar Phys.* **20**, 3
- Mein, P., Mein, N., Malherbe, J. M., and Damé, L.: 1987, *Astron. Astrophys.* **177**, 283
- Narasimha, D.: 1993, in T. M. Brown (Ed.), *GONG1992: Seismic Investigation of the Sun and Stars*, ASP Conf. Series 42, p. 127
- Nordlund, Å.: 1982, *Astron. Astrophys.* **107**, 1
- Nordlund, Å. and Dravins, D.: 1990, *Astron. Astrophys.* **228**, 155
- November, L. J.: 1989, *Astrophys. J.* **344**, 494
- Noyes, R. W.: 1967, in R. N. Thomas (Ed.), *Aerodynamic Phenomena in Stellar Atmospheres*, IAU Symp. 28, Academic Press, London, p. 293
- Noyes, R. W. and Leighton, R. B.: 1963, *Astrophys. J.* **138**, 631
- Provost, J. and Mein, N.: 1979, *Solar Phys.* **64**, 43
- Punetha, L. M.: 1974, *Bull. Astron. Inst. Czech.* **25**, 212
- Rammacher, W. and Ulmschneider, P.: 1992, *Astron. Astrophys.* **253**, 586
- Roellig, T. L., Becklin, E. E., Jefferies, J. T., Kopp, G. A., Lindsey, C. A., Orrall, F. Q., and Werner, M. W.: 1991, *Astrophys. J.* **381**, 288
- Rutten, R. J.: 1993, in C. Mattok (Ed.), *Targets for Space-Based Interferometry*, Proceedings ESA Colloquium (Beaulieu), ESA SP-354, ESA Publ. Div., ESTEC, Noordwijk, p. 163
- Rutten, R. J. and Uitenbroek, H.: 1991a, *Solar Phys.* **134**, 15
- Rutten, R. J. and Uitenbroek, H.: 1991b, in P. Ulmschneider, E. R. Priest, and R. Rosner (Eds.), *Mechanisms of Chromospheric and Coronal Heating*, Proc. Heidelberg Conf., Springer Verlag, Berlin, p. 48
- Salucci, G., Bertello, L., Cavallini, F., Ceppatelli, G., and Righini, A.: 1994, *Astron. Astrophys.* **285**, 322
- Schmitz, F., Ulmschneider, P., and Kalkofen, W.: 1985, *Astron. Astrophys.* **148**, 217
- Schrijver, C. J.: 1994, in R. J. Rutten and C. J. Schrijver (Eds.), *Solar Surface Magnetism*, NATO ASI Series C433, Kluwer, Dordrecht, p. 271
- Schrijver, C. J., Zwaan, C., Balke, A. C., Tarbell, T. D., and Lawrence, J. K.: 1992, *Astron. Astrophys.* **253**, L1
- Sivaraman, K. R.: 1991, in P. Ulmschneider, E. Priest, and B. Rosner (Eds.), *Mechanisms of Chromospheric and Coronal Heating*, Heidelberg Conference, Springer Verlag, Berlin, p. 44
- Sivaraman, K. R. and Livingston, W. C.: 1982, *Solar Phys.* **80**, 227

- Skartlien, R.: 1994, *Dynamics in stellar chromospheres*, Cand. Scient. Thesis, Inst. Theor. Astrophys. Oslo
- Skumanich, A., Lean, J. L., White, O. R., and Livingston, W. C.: 1984, *Astrophys. J.* **282**, 776
- Solanki, S. K., Bruls, J. H. M. J., Steiner, O., Ayres, T., Livingston, W., and Uitenbroek, H.: 1994a, in R. J. Rutten and C. J. Schrijver (Eds.), *Solar Surface Magnetism*, NATO ASI Series C433, Kluwer, Dordrecht, p. 91
- Solanki, S. K., Livingston, W., and Ayres, T.: 1994b, *Science* **263**, 64
- Spruit, H. C., Nordlund, Å., and Title, A. M.: 1990, *Ann. Rev. Astron. Astrophys.* **28**, 263
- Stein, R. F. and Nordlund, Å.: 1989, *Astrophys. J. Lett.* **342**, L95
- Stein, R. F. and Schwartz, R. A.: 1972, *Astrophys. J.* **177**, 807
- Steiner, O., Knölker, M., and Schüssler, M.: 1994, in R. J. Rutten and C. J. Schrijver (Eds.), *Solar Surface Magnetism*, NATO ASI Series C433, Kluwer, Dordrecht, p. 441
- Straus, T., Deubner, F.-L., and Fleck, B.: 1992, *Astron. Astrophys.* **256**, 652
- Suemoto, Z., Hiei, E., and Nakagomi, Y.: 1987, *Solar Phys.* **112**, 59
- Suemoto, Z., Hiei, E., and Nakagomi, Y.: 1990, *Solar Phys.* **127**, 11
- Sutmann, G. and Ulmschneider, P.: 1994a, *Astron. Astrophys.* in press
- Sutmann, G. and Ulmschneider, P.: 1994b, *Astron. Astrophys.* in press
- Title, A. M., Tarbell, T. D., Topka, K. P., Ferguson, S. H., Shine, R. A., and the SOUP Team: 1989a, *Astrophys. J.* **336**, 475
- Title, A. M., Tarbell, T. D., Topka, K. P., Ferguson, S. H., Shine, R. A., and the SOUP Team: 1989b, in R. J. Rutten and G. Severino (Eds.), *Solar and Stellar Granulation*, NATO ASI Series C-263, Kluwer, Dordrecht, p. 225
- Uitenbroek, H., Noyes, R. W., and Rabin, D.: 1994, *Astrophys. J. Lett.* in press
- Ulmschneider, P.: 1990, in G. Wallerstein (Ed.), *Cool Stars, Stellar Systems and the Sun*, Proc. Sixth Cambridge Workshop, Astron. Soc. Pac. Conference Series, Volume 9, p. 3
- Ulmschneider, P.: 1991, in P. Ulmschneider, E. Priest, and B. Rosner (Eds.), *Mechanisms of Chromospheric and Coronal Heating*, Heidelberg Conference, Springer Verlag, Berlin, p. 328
- Ulrich, R. K.: 1970, *Astrophys. J.* **162**, 933
- Vaughan, A. H., Preston, G. W., and Wilson, O. C.: 1978, *Publ. Astron. Soc. Pac.* **90**, 267
- Wannier, P. G., Hurford, G. J., and Seielstad, G. A.: 1983, *Astrophys. J.* **264**, 660
- White, S. M. and Kundu, M. R.: 1994, in D. M. Rabin, J. T. Jefferies, and C. Lindsey (Eds.), *Infrared Solar Physics*, Proc. IAU Symp. 154, Kluwer, Dordrecht, p. 167
- Zirin, H.: 1974, *Solar Phys.* **38**, 91
- Zirin, H.: 1988, *Astrophysics of the Sun*, Cambridge University Press, Cambridge, Great Britain

# RADIATION SHOCK DYNAMICS IN THE SOLAR CHROMOSPHERE – RESULTS OF NUMERICAL SIMULATIONS

MATS CARLSSON

*Institute of Theoretical Astrophysics, P.O.Box 1029 Blindern, N-0315 Oslo, Norway*

and

ROBERT F. STEIN

*Department of Physics & Astronomy, Michigan State University, East Lansing, MI 48824, USA*

## Abstract.

We report results from self-consistent non-LTE radiation hydrodynamics simulations of the propagation of acoustic waves through the solar chromosphere.

It is found that enhanced chromospheric emission, which corresponds to an outwardly increasing semi-empirical temperature structure, can be produced by wave motions without any increase in the mean gas temperature. Thus, despite long held beliefs, the sun may not have a classical chromosphere in magnetic field free internetwork regions.

The dynamic formation of continuum radiation is described in some detail. Concepts that work well in static models do not necessarily work in the dynamic chromosphere. The contribution function for the intensity may be bimodal with one peak around  $\tau_\nu = 1$  and another at a shock at smaller optical depth. The mean height of formation will then be between those regions and have no relation to either formation region.

Above the photosphere, the source function is so decoupled from the Planck function that variations in intensity can *not* be taken as a proxy for gas temperature variations. The emergent intensity does not show the discontinuous rise signature of shock waves even for the continua formed where the shocks are strong. Even in the photosphere a one-to-one correspondence between intensity variation and gas temperature variation is not possible because of the dependence of the formation height on the opacity and therefore on the temperature.

The modification of velocity amplitude and phase as a function of frequency and depth in the atmosphere is described with a transfer function. This function is found to be rather insensitive to the input velocity field in the photosphere. By using the derived transfer function it is possible to construct piston velocities that give photospheric velocities that match observed Doppler shifts.

The simulations closely match the observed behaviour of CaII H<sub>2</sub>V bright grains. The formation of bright grains is described in detail and both the brightness and the wavelength position of the grains are explained. It is found that the grain pattern is completely set by the velocity pattern of the piston. The frequency components around 3 minute periods are found to be most important but with significant modulation of the grain behaviour from the low frequency component of the velocity field. The strength of grains is not directly proportional to the photospheric 3 minute power but a result of interference between many modes.

**Key words:** Hydrodynamics, Radiative transfer, Shock Waves, Sun: chromosphere

## 1. Introduction

The solar atmosphere is a dynamic radiating medium and many of its outstanding problems require radiation-hydrodynamics for their investigation. Detailed comparison of the evolution of line profiles observed with high spatial and temporal reso-

lution with self-consistent radiation-hydrodynamic simulations provides a means for developing diagnostics for atmospheric motions.

We have developed a code that is capable of such a self-consistent radiation-hydrodynamic treatment under solar chromospheric conditions with the important radiative transitions treated in non-LTE. Earlier schematic studies using sinusoidal monochromatic driving velocity fields (Carlsson and Stein, 1992) are here expanded to driving velocity fields that reproduce observed Doppler shifts in photospheric lines. These simulations are used to show that the whole concept of a semistatic non-magnetic chromosphere is completely misleading. We also focus on the behaviour of the Ca II line profiles, because new high quality data are now available (see other contributions in these proceedings) and the question as to what drives the appearance of  $K_2V$  bright grains has been much debated recently (*e.g.*, Rutten and Uitenbroek, 1991, Rammacher and Ulmschneider, 1992, Rossi *et al.*, 1992).

The layout of the paper is as follows: In section 2 we describe the methods used and in section 3 we describe the results with a detailed analysis of the formation of continuum radiation in section 3.1, the equivalent semi-empirical atmosphere in section 3.2 and the atmospheric transfer function in section 3.3. The formation of  $H_2V$  and  $K_2V$  bright grains is discussed in section 3.4. The results are discussed in section 4 and the conclusions are given in section 5. Phase relations between intensity and velocity for the calcium lines are discussed in a companion paper.

## 2. Method

We solve the one-dimensional equations of mass, momentum and energy conservation together with the non-LTE radiative transfer and population rate equations, implicitly on an adaptive mesh. The radiative transfer is treated using Scharmer's method (Scharmer, 1981, Scharmer and Carlsson, 1985, Carlsson, 1986). The advection terms are treated using Van Leer's (1977) second order upwind scheme to ensure stability and monotonicity in the presence of shocks. An adaptive mesh is used (Dorf and Drury, 1987) in order to resolve the regions where the fluid properties are changing rapidly (such as in shock fronts). The equations are solved implicitly to ensure stability in the presence of radiative energy transfer, and to have the time steps controlled by the rate of change of the variables and not by the Courant time for the smallest zones.

We include 6 level model atoms for hydrogen and singly ionized calcium. Other continua are treated as background continua in LTE, using the Uppsala atmospheres program (Gustafsson, 1973). Our initial atmosphere is in radiative equilibrium without line blanketing above the convection zone (for the processes we consider) and extends 100 km into the convection zone, with a time constant divergence of the convective energy flux (on a column mass scale) calculated with the Uppsala code without line blanketing. Basic quantities for the initial atmosphere are shown in Fig. 1.

Waves are driven through the atmosphere by a piston located at the bottom of the computational domain (100 km below  $\tau_{500} = 1$ ) whose velocity is taken from a 3750 second sequence of Doppler shift observations in an Fe I line at  $\lambda 396.68$  nm in the wing of the Ca H-line (Lites *et al.*, 1993). Two procedures have been used to

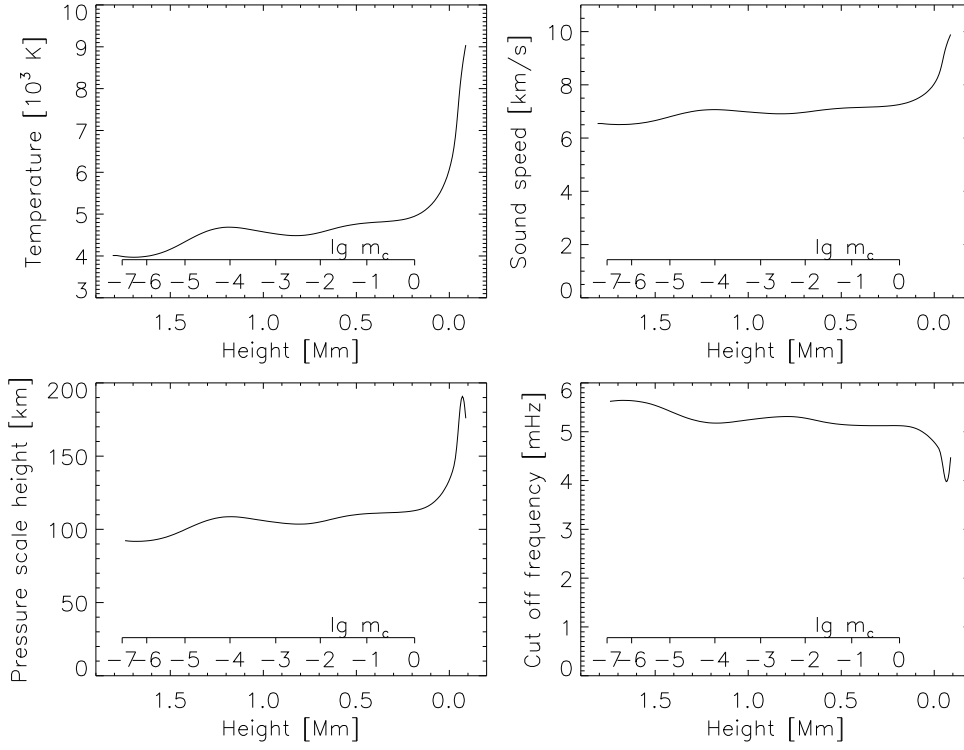


Fig. 1. Temperature, sound speed, pressure scale height and acoustic cut off frequency as functions of height in the starting atmosphere.  $\lg(\text{column mass})$  is given as a secondary scale.

transform these observed Doppler shifts into a piston velocity. Originally the Doppler shifts were just scaled with 0.2, which was based on a computed amplification of the amplitude of a monochromatic three-minute wave from the height of the piston to the static height of formation of the iron line ( $\approx 260$  km above  $\tau_{500} = 1$ ). This piston velocity in the simulation produces too little low frequency power at the height of 260 km to give the Doppler shifts observed there. The reason is that the amplification is not constant with frequency, and in addition, there is a zero phase-shift for non-propagating low frequency modes and a non-zero phase-shift at higher frequencies due to the propagation time between the two heights. The second procedure takes these effects into account by using the first simulation to calculate a transfer function,  $H$ , for the atmosphere:

$$F[v_{260\text{km}}] = H F[v_{100\text{km}}], \quad (1)$$

where  $F[v]$  denotes the Fourier transform of the velocity. The piston velocities are then obtained as

$$v_{\text{piston}} = F^{-1}(H^{-1} F(v_{\text{Fe}})). \quad (2)$$

This procedure gives velocities at 260 km that quite closely match the observed Doppler shifts in the iron line. See Section 3.3 for a discussion of the transfer function of the atmosphere in the simulations.

There is a transmitting boundary condition at the top of the computational domain.

The microturbulence broadening was set to a constant 2 km/s throughout the atmosphere.

After this dynamic calculation is completed, we then recalculate the behavior of the C I, Si I, Mg I and Al I continua in non-LTE. These continua are thus included in the energy balance in the dynamic calculation in LTE and the non-LTE calculation is done for each snap-shot of the dynamic simulation with no back-coupling on the energy balance. The overlap between continua treated in non-LTE is treated iteratively.

The model atoms of C I, Si I, Mg I and Al I are similar to those used in the VAL series of papers (Vernazza, Avrett & Loeser 1973, 1976, 1981) but with the photoionization cross-sections updated with data from Mathisen (1984) and the opacity project (see Seaton *et al.*, 1994 and references therein). All other opacity sources and electron donors are treated in LTE.

## 2.1. SEMI-EMPIRICAL ATMOSPHERE

To compare the physics in the dynamical simulation with the conclusions we would draw from a classical analysis of the time-average of the simulation, we analyze the dynamical simulation in a way similar to the construction of the VAL3 models. The time averaged intensity as a function of wavelength from the simulation is taken as the quantity to be reproduced by a semi-empirical model atmosphere. For an assumed temperature structure the equations of hydrostatic equilibrium, statistical equilibrium and radiative transfer are solved and the computed intensities are compared with the time average from the dynamical atmosphere. The difference is fed into an automatic scheme (Skartlien, 1994) that calculates the adjustment to be made to the semi-empirical temperature structure and the process is iterated to convergence.

This optimization problem is rather ill conditioned due to the width of the intensity contribution functions; any change on a scale substantially smaller than this width will not change the outgoing intensity. For this reason a smoothness criterion has been imposed on the semi-empirical temperature; above the classical temperature minimum the difference between a radiative equilibrium temperature structure and the semi-empirical temperature structure is described with a fifth order polynomial. Another reason for the ill-conditioned optimization problem is the fact that some height ranges are not represented with radiation formed there; in particular this is true for the heights between the formation heights of the Lyman continuum and the carbon continuum.

The atoms treated in non-LTE are the same as when calculating the time average of the intensity from the dynamic simulation: hydrogen, carbon, silicon, magnesium and aluminum.

Short-ward of infrared and mm wavelengths only in the UV are continua formed above the position of the temperature minimum in the VAL models. The semi-empirical temperature structure is thus determined by the time averaged intensities in the UV from 1500 Å (formed around the VAL temperature minimum) to the Lyman continuum (formed in the upper chromosphere in the VAL models).

The final semi-empirical temperature structure is typically able to reproduce the time averaged intensity to within 20 K in radiation temperature above 100 nm and to within 100 K in the Lyman continuum below 91.2 nm.

### 3. Results

#### 3.1. FORMATION OF CONTINUUM RADIATION

Our inferences about the solar chromosphere are based on our analysis of the light we receive. To properly interpret our observations we need to know how that light is produced. In this section we discuss the formation of the continuum radiation at four wavelengths (the dominant bound-free opacity source given in parenthesis): 207 nm (Al I), 152 nm (Si I), 110 nm (C I) and 91.2 nm (Lyman continuum). The intensities discussed below are for the wavelength just short-ward of the respective bound-free opacity edge. These continua span a range of heights of formation and ionization potentials. We will see that concepts that work well in the static photosphere do not necessarily work in the dynamic chromosphere.

The contribution to the emergent intensity from a location  $(z, z + dz)$  can be written

$$\delta I_\nu = [S_\nu][\exp(-\tau_\nu)][\sigma_\nu][ndz], \quad (3)$$

a product of the source function, an attenuation factor, the cross-section and the column density of emitting atoms.

The source function is more or less strongly coupled to the Planck function which is very temperature sensitive in the UV, varying as  $\exp(-\text{const}/T)$ , but varies linearly with temperature in the mm wavelength range.

In a dynamic atmosphere, with shocks present, the contribution function for the intensity may be bimodal, with one peak around  $\tau_\nu = 1$  and another at a shock at smaller optical depth. The shock may make a large contribution to the intensity because the source function can become extremely large and outway the small number density of emitting atoms at small optical depth. This is especially true at short wavelengths where the shock temperature increase gives an exponential increase in the Planck function. In this case the mean height of formation may well be somewhere between the shock and optical depth one and have no relation to either formation region. With this in mind we now consider the detailed behavior of the Al I, Si I C I and H I continua.

Figures 2–3 show the formation of the continuum intensities in the four continua at two different times in the dynamical simulation. The temperature is shown together with the source function, the contribution function to the intensity, the radiation temperature of the emergent intensity and the height and monochromatic optical depth scales.

Figure 4 gives the evolution in time over a short part of the full dynamic simulation of 7500 seconds.

The Al I continuum with its edge at 207 nm is formed deep, around  $\lg \tau_{500} = -0.66$  at a height of 92 km. The mean depth of formation is below  $\tau_\nu = 1$  because the contribution function gives more weight to larger depths due to the outward temperature drop. Aluminum has a low ionization potential, so it is nearly all ionized and Al I is not the main ionization stage. This makes the opacity very temperature

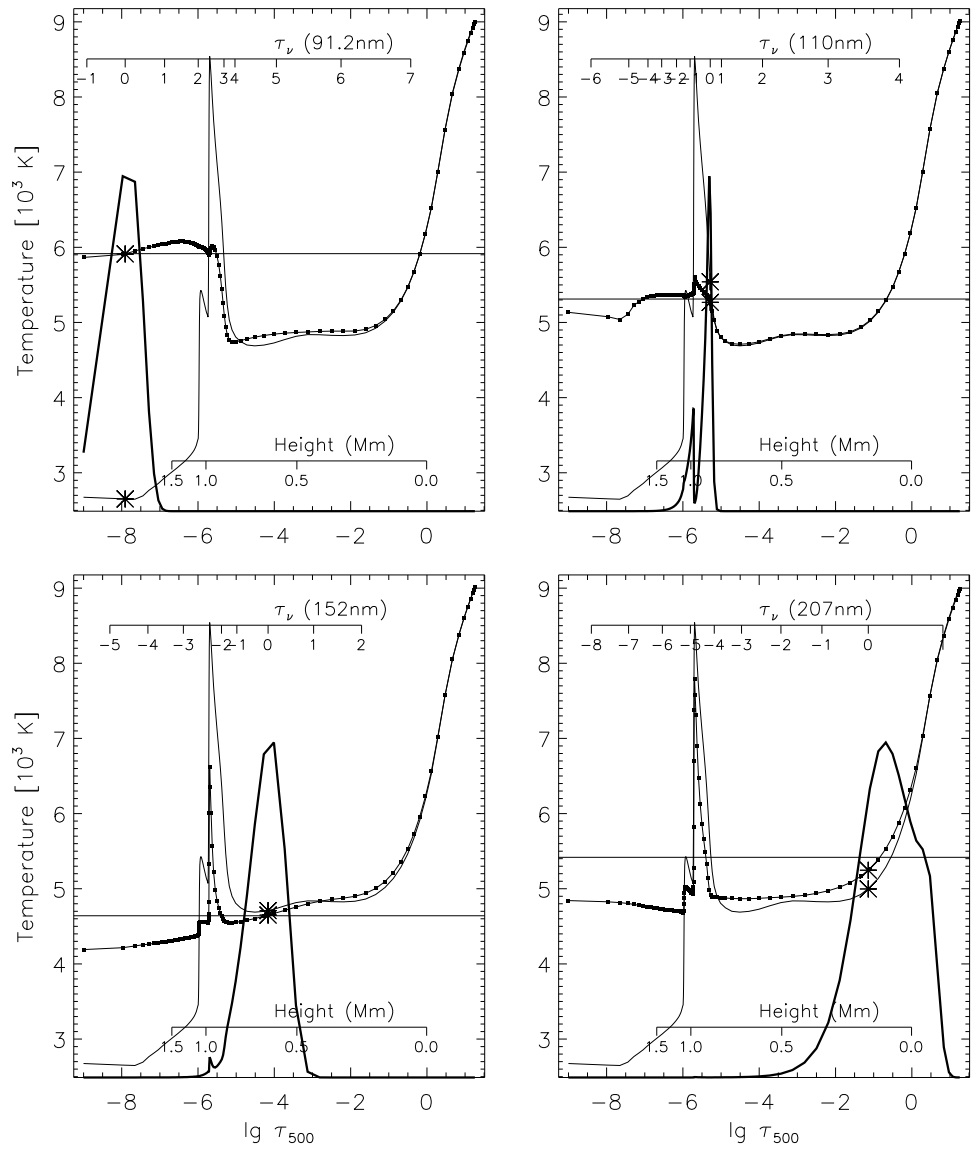


Fig. 2. Snapshot from the dynamical simulation at  $t=1530$  s. Temperature (thin solid line, same in all four panels), source function (dotted) and the contribution function to the intensity (thick solid) as functions of  $\lg \tau_{500}$ . The temperature and the source function at  $\tau_\nu = 1$  are marked with asterisks. The radiation temperature of the outgoing intensity is shown as a horizontal line. Four different wavelengths are shown corresponding to the Lyman continuum at 91.2 nm (top left panel), C I continuum at 110 nm (top right), Si I continuum at 152 nm (bottom left) and the Al I continuum at 207 nm (bottom right).

sensitive. The source function is slightly larger than the Planck function due to the non-LTE over-ionization. The source function at  $\tau_\nu = 1$  is thus above the Planck function at that point and the emergent intensity is even higher due to the mean

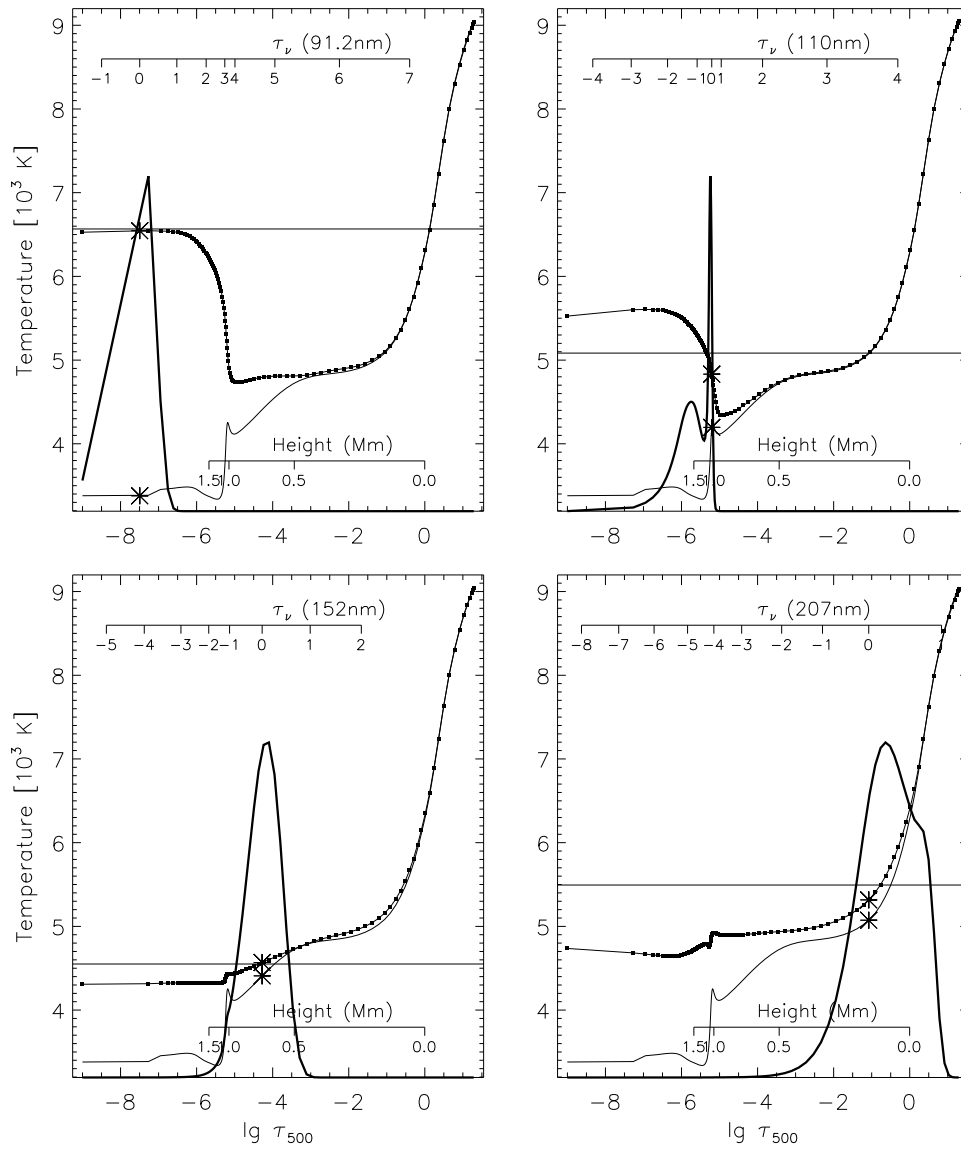


Fig. 3. As Fig. 2 but at  $t=1610$  s.

formation depth being below  $\tau_\nu = 1$ . These effects do not vary much in time and the emergent intensity, the source function and the Planck-function thus vary in phase (Fig. 4). However, because of the temperature sensitivity of the ionization stage and hence opacity, an increase in temperature produces further ionization, which leads to a smaller opacity, so one sees in deeper to yet higher temperature. Thus the variation in radiation temperature will be larger than the variations in gas temperature at the mean formation height; the rms of the radiation temperature in the simulation is

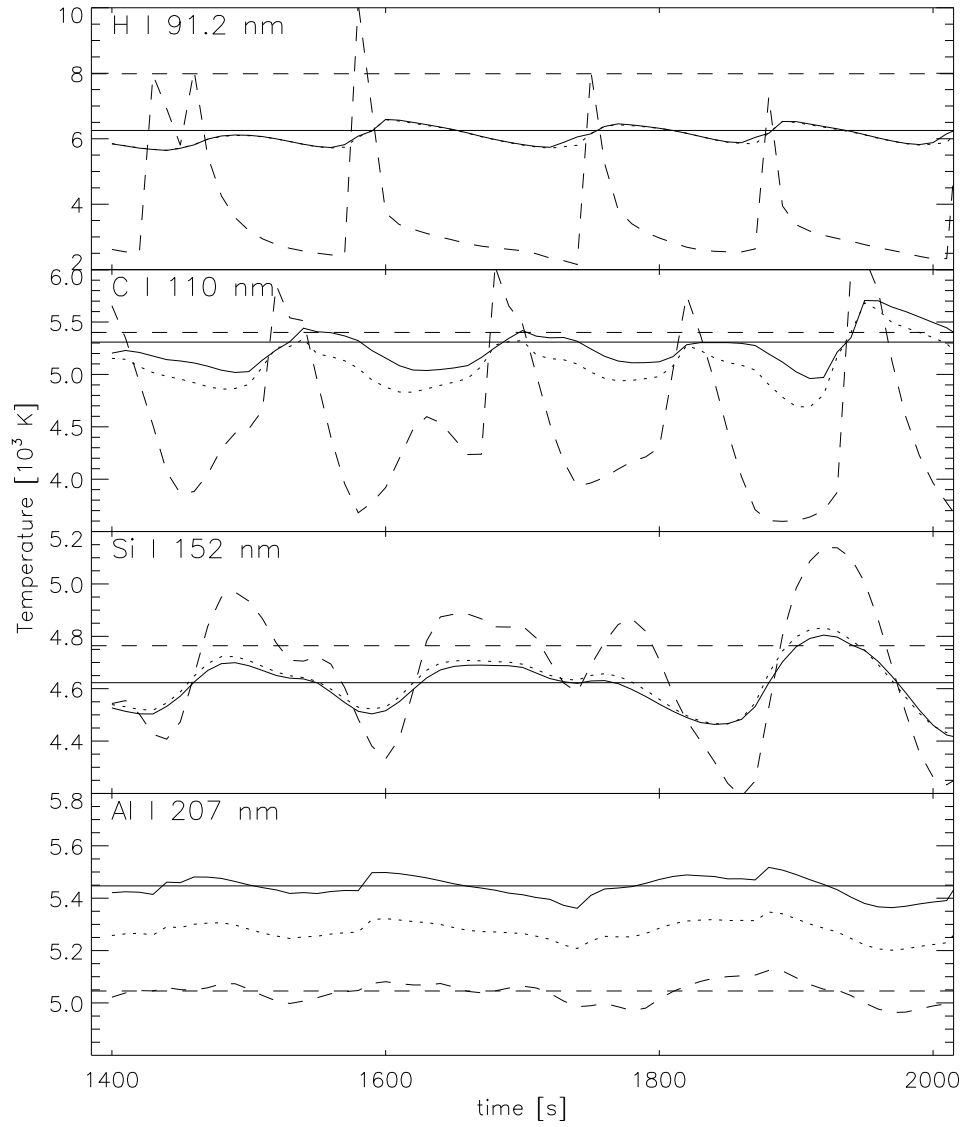


Fig. 4. The radiation temperature of the outgoing intensity (solid), the source function at  $\tau_\nu = 1$  (dotted) and the temperature at  $\tau_\nu = 1$  (dashed) as functions of time for a small part of the dynamical simulation for four wavelengths. The horizontal lines show the radiation temperature of the mean of the outgoing intensity (solid) and of the mean of the Planck function (dashed) with the mean taken over this part of the simulation. The means from the complete simulation will be slightly different. The non-linear averaging is clearly shown with the radiation temperature of the intensity mean being close to the maximum intensity and likewise for the Planck function. The source function varies much less than the Planck function due to the non-LTE decoupling. The radiation temperature of the outgoing intensity does not show the shock signature of a discontinuous rise for the same reason

40K while the rms of the gas temperature at a *fixed* height of 100km is 17K. The rms variation in mean formation height is 0.04 in  $\lg \tau_{500}$  corresponding to 7 km.

The silicon continuum at 152 nm is formed around  $\lg \tau_{500} = -4.3$  at a height of 648 km. The rms variation in the mean height of formation is 0.11 in  $\lg \tau_{500}$  corresponding to 49 km. Silicon has a moderate ionization potential. Hence, near the formation depth, silicon is  $\approx 80\%$  ionized. Due to the lower temperatures in the dynamic model, compared with a classical model with a chromosphere, and the temperature sensitivity of the silicon ionization, the formation height is substantially higher than in a semi-empirical model. The source function and Planck function are nearly uniform in the formation region, because it is below the region where shocks significantly modify the temperature structure (and hence the source function) and above the region of decreasing photospheric temperatures. This layer is near the region where shocks create an instantaneous temperature increase as they pass through. The intensity is produced close to  $\tau_\nu = 1$  (4), and the classical contribution function there dominates the intensity formation. There may be a secondary peak in the contribution function at a shock at smaller optical depth, but such secondary maxima always make smaller contributions to intensity. As a result, fluctuations in the radiation temperature follow the thermal temperature at  $\tau_\nu = 1$ . However, the radiation temperature fluctuations have a smaller amplitude (rms of 86 K) than those in the gas temperature (rms of 210 K) due to the decoupling of the non-LTE source function and the Planck function.

The carbon continuum at 110 nm is formed at  $\lg \tau_{500} = -5.6$ , just below where shocks become strong. The rms variation in the mean height of formation is 0.32 in  $\lg \tau_{500}$  corresponding to 168 km. Carbon has a high ionization potential, so is nearly all neutral there. Since this is near the level of strong shock formation, the source function responds to both the high temperatures at the shock and the low temperatures in their wake. However, the source function varies much less than the Planck function, because it is controlled by radiation, not by collisions. The intensity contribution function is often bi-modal, with one peak near  $\tau_\nu = 1$  and the other at the shock (Figs. 2–3). The radiation temperature is generally above the gas temperature at  $\tau_\nu = 1$  and does not dip as low. Only when a strong shock is formed by merging of shocks at small heights does the temperature in the wake fall low enough to make the source function follow. The radiation temperature of the emergent intensity shows a large rms variation of 165 K. The gas temperature at  $\tau_\nu = 1$  shows an rms variation of 636 K.

The Lyman continuum at 91.2 nm is formed close to the top of the computational domain. The monochromatic optical depth at the top boundary is around 0.1 and the emergent intensities will be affected by the treatment of the matter leaving the computational domain and by the absence of a magnetic canopy in the simulations (see Section 4). Keeping this in mind, the continuum radiation is formed around  $\lg \tau_{500} = -8$  with an rms variation of 0.27 in  $\lg \tau_{500}$  corresponding to 59 km in height. The source function is almost completely decoupled from the Planck function; this gives a much smaller variation in the radiation temperature of the emergent intensity (rms of 256 K) than in the gas temperature at  $\tau_\nu = 1$  (rms of 1910 K). The gas temperature shows a rapid almost discontinuous rise when the shocks pass while the radiation temperature shows no such shock signature due to the decoupling of

the source function from the Planck function. The timescale for hydrogen ionization/recombination is long at the height of formation of the Lyman continuum. The recombination then takes place behind the shocks leading to a maximum radiation temperature after the maximum gas temperature at  $\tau_\nu = 1$ .

Continua formed in the photosphere, e.g. AlI with the edge at 207 nm, and up to about 0.5 Mm, e.g. SiI with the edge at 152 nm, thus have contribution functions peaked near  $\tau_\nu = 1$  and have no secondary maxima at the height where shocks exist because the number of their atoms at that height is extremely small. The C I continuum with the edge at 110 nm is formed close to where shocks form and often exhibits a bimodal contribution function (Figs. 2–3). Even though the number of atoms at shock forming heights is small, the exponential temperature sensitivity of the Planck function outweighs this factor.

Above the photosphere, the source function is so decoupled from the Planck function that variations in intensity can *not* be taken as a proxy for gas temperature variations (Fig. 4). Even in the photosphere such a one-to-one correspondence between intensity variation and gas temperature variation is not possible because of the dependency of the formation height on the opacity and therefore on the temperature.

### 3.2. SEMI-EMPIRICAL ATMOSPHERE

Figure 5 shows the time average of the temperature as a function of height in the dynamical simulation as a thick solid line. This average dynamic temperature structure shows no chromospheric rise. The corresponding semi-empirical temperature structure (dashed) is obtained by treating the temperature as a function of height as a free parameter and iterating to get the best possible fit between the intensities calculated from the semi-empirical model and the time average of the intensity as a function of wavelength calculated from the dynamical simulation (see Section 2.1). Also shown in the figure are the range of temperatures in the simulation (thin solid lines), the starting model for the dynamical simulation (dotted) and the semi-empirical model FALA constructed to reproduce the solar dark internetwork regions (dot-dashed) (Fontenla *et al.*, 1993).

The striking feature of Fig. 5 is that the time average of the temperature as a function of height in the dynamical simulation shows *no chromospheric temperature rise* while the best match semi-empirical model has a classical chromospheric temperature rise.

The temperature averaging in the dynamic simulation was done for given heights but the result is independent of the averaging procedure. The same monotonic temperature decrease with height is obtained by averaging on fixed column masses (Lagrangian grid). Averaging the thermal energy instead of the temperature again gives the same result.

Why is a semi-empirical temperature rise needed to reproduce the time-averaged intensities? Although the diagnostic continua were calculated in non-LTE as explained in Section 2.1, we will nevertheless start this discussion with a test case where all diagnostic continua were calculated in LTE.

In LTE one would expect the best match semi-empirical temperature to be close to the maximum temperature due to the exponential temperature sensitivity of the Planck function in the UV. This is not the case — the semi-empirical temperature

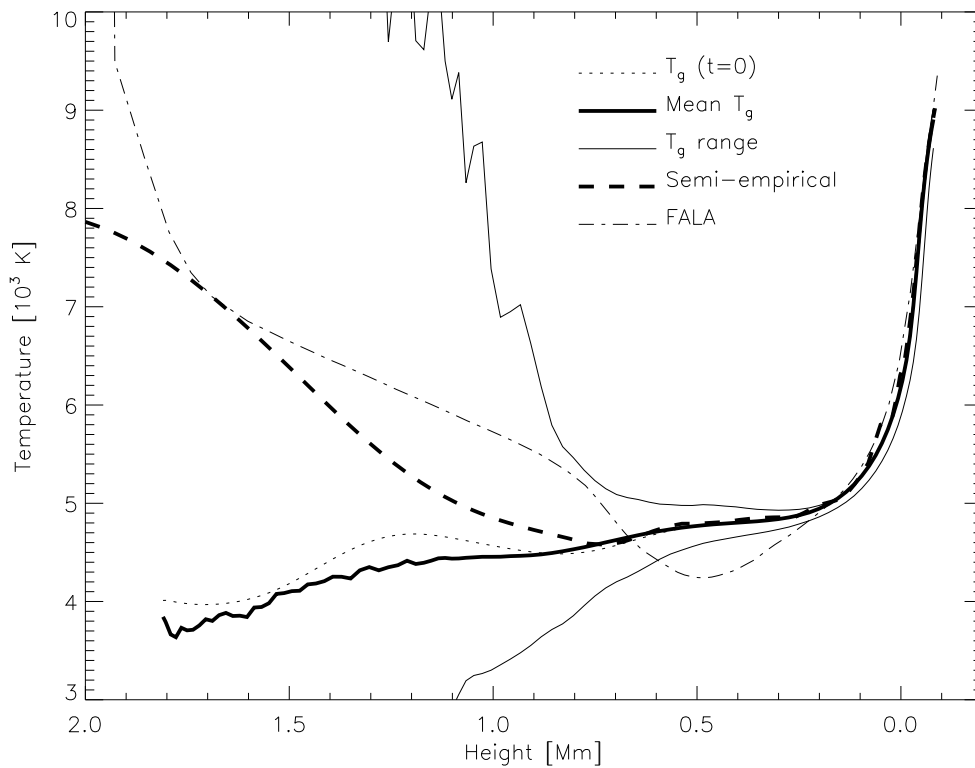


Fig. 5. Time average of the temperature in the dynamical simulation (thick solid), the range of temperatures in the simulation (thin solid), the semi-empirical model that gives the best fit to the time average of the intensity as a function of wavelength calculated from the dynamical simulation (thick dashed), the starting model for the dynamical simulation (dotted) and the semi-empirical model FALA (dot-dashed). The maximum temperatures are only reached in narrow shock spikes of short duration. The semi-empirical model giving the same intensities as the dynamical simulation shows a chromospheric temperature rise while the mean temperature in the simulation does not.

lies much lower than the maximum shock temperatures even in LTE. This is partly because the maximum temperatures occur in very narrow shock spikes of short duration and also because the width of the contribution function smears out the influence of the spikes on the intensities. The radiation temperature of the average intensity is above the average temperature, however, because of the exponential temperature dependency of the Planck-function. This results in a semi-empirical temperature rise.

In non-LTE the effects are much the same. The source function is partly decoupled from the Planck-function and shows much less variation with time (see Fig. 4). However, the non-linear weighting of the higher temperatures is similar to the LTE-case and one gets a semi-empirical temperature rise. The intensities thus vary less and have a different mean radiation temperature than in the LTE case. Despite these differences, the best fit semi-empirical temperature structure is very similar in LTE and non-LTE, even though the mean intensities are different.

The mechanisms operating in the Lyman continuum are different from the other continua due to the slow ionization/recombination rates. These effects have been neglected for the other continua since these model atoms were not included self-consistently in the dynamic calculation (see Section 4 for a discussion of possible consequences of this neglect). At a given time the viscous dissipation in the shocks together with the pressure work leads to a high temperature. This shock spike is very strong because the long timescales for hydrogen ionization/recombination prevents the energy from going into ionization energy (Carlsson and Stein, 1992). Hydrogen is ionized further back into the post-shock region lowering the temperature. Even further back, the recombination takes place releasing the energy in the form of radiative cooling. Integrated over time at a given height, the viscous dissipation is balanced by the radiative cooling and there is no increase in the thermal energy. There is, however, an increased radiation compared with the radiative equilibrium starting at atmosphere due to the radiative cooling. The slow hydrogen ionization/recombination thus increases the intensity and drastically lowers the amplitude of the intensity variations.

### 3.3. VELOCITY TRANSFER FUNCTION

The velocity spectrum as a function of frequency changes with height, both in amplitude and phase. The velocity amplitude of propagating waves increases with height in a stratified atmosphere to maintain a constant flux as the density decreases. Damping reduces this amplitude increase. Propagating modes also show a phase shift due to their finite phase speed. For evanescent modes one expects more damping but no change in phase as a function of height.

We describe the change in the velocity spectrum in the simulations with a transfer function,  $H_{z_1, z_2}$ , defined as

$$F[v_{z_2}] = H_{z_1, z_2} F[v_{z_1}], \quad (4)$$

where  $F[v_{z_1}]$  denotes the Fourier transform of the velocity at height  $z_1$ .

The transfer function is thus a complex valued function where the absolute value gives the ratio of velocity amplitude between the two heights and the phase gives the  $(v_{z_2} - v_{z_1})$  phase difference.

Figure 6 shows the velocity transfer function over height intervals of 100 km as a function of height in the atmosphere. The large spread in phase and amplitude amplification in the bottom panels is due to low power at high frequencies at a height of  $-70$  km. The phase difference plots show the expected behaviour with no phase difference in the evanescent regime below the cut-off frequency (which varies from 4 mHz at the bottom to 5 mHz at 300 km height, see Fig.1). The phase difference for propagating waves is what is expected from a phase speed asymptotically approaching the sound speed for high frequencies. The velocity amplitude in the evanescent regime is nearly constant with height indicating strong damping, since for undamped waves the amplification factor would be 1.3–1.7 over 100 km with a pressure scale height of 110–190 km. For higher frequencies, the amplification approaches the undamped value.

The transfer function from the height of the piston to the formation height of the Fe I line at  $\lambda 396.68$  nm (about 260 km) was used to compute the piston velocity (see

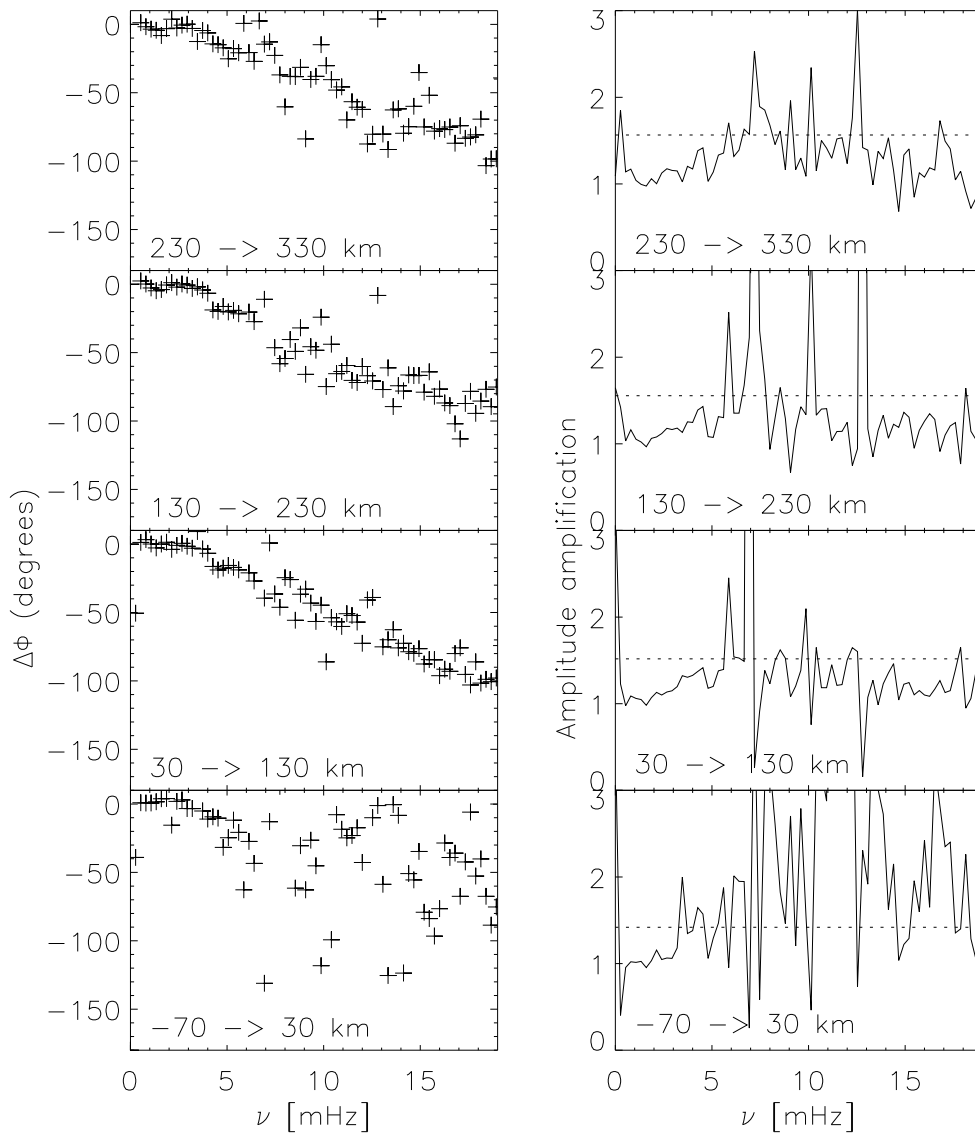


Fig. 6. Velocity transfer function over height intervals of 100 km. The large spread in phase and amplitude amplification in the bottom panels is due to low power at high frequencies at a height of  $-70$  km. The dotted line in the right panel shows the undamped amplification factor  $\exp\Delta z/2H$ .

section 2). Provided the transfer function is independent of the piston velocities, this procedure should recover the Fe I Doppler shifts as the velocity at the height 260 km in the model. The transfer function from two different velocity fields is shown in Fig. 7 together with the observed Doppler shifts and the velocities in the simulations at the height 260 km. The transfer functions for the two different velocity fields are rather similar at low frequencies. At high frequencies there is a lot of noise due to

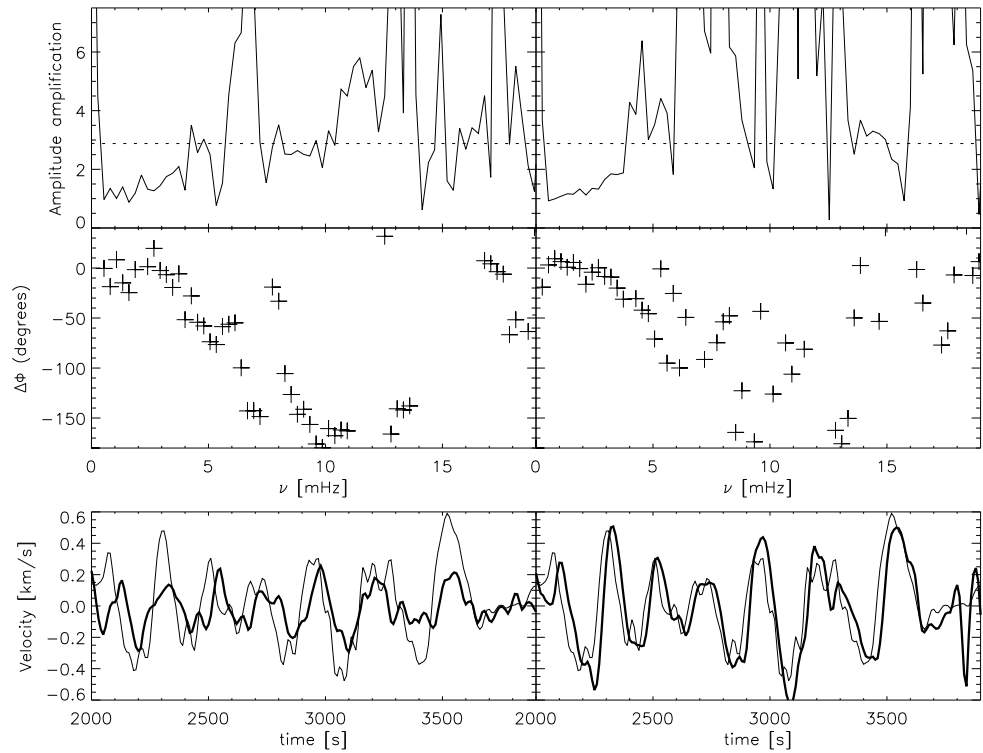


Fig. 7. Velocity transfer function from the height of the piston to the formation height of the observed FeI line at  $\lambda 396.68$  nm (about 260 km) with velocity amplification in the top panels (dotted line: undamped amplification factor of  $\exp \Delta z / 2H$ ), phase shift in the middle panels and the velocity at a height of 260 km in the simulation (thick) compared with the observed Doppler shift in the FeI line (thin). The left hand panels show the results from a piston velocity taken to be the observed FeI Doppler shifts scaled by 0.2. The right hand panels show the results from a piston velocity calculated with the help of the transfer function of the left panel. The observed Doppler shifts are quite well recovered except for a remaining phase shift of about 22 seconds.

the small power at those frequencies at the height of the piston. The piston velocities used for the computations shown in the left hand panels contain more high frequency power and less low frequency power than the piston velocities for the computations shown in the right hand panels. This is clearly visible in the amount of noise in the transfer function.

Just scaling the observed Doppler shifts with a factor of 0.2 gives too little power in the evanescent regime. Using this transfer function to adjust the piston velocities gives a good recovery of the Doppler shifts (Fig. 7, lower panels). Note, however, that the computed velocities lag the observed Doppler shifts by about 22 seconds.

The velocity amplitude at 260 km height is about 10% of the local sound speed. Higher up in the atmosphere we would expect the concept of a transfer function as a property of the atmosphere to break down because the large amplitude perturbations modify the atmosphere significantly.

### 3.4. FORMATION OF $H_{2V}$ BRIGHT GRAINS

The quasi-periodic emission in the core of the H and K lines of ionized calcium is asymmetric with often strong emission on the violet side of the line center (so called  $H_{2V}$  and  $K_{2V}$  bright grains) and seldom any emission on the red side. This asymmetry is explained by the correlation between velocity and temperature. We will here go further, in an attempt to clarify what factors influence the separation of the  $H_2$  peaks and where they are formed. We will also analyze different simulations and show that the occurrence of grains is determined wholly by the velocity field and *not* by the previous history of the atmosphere. Finally, we will reveal the characteristics of the photospheric velocity field that are sufficient to create bright grains. In the simulations we will show results for the H-line in order to be able to compare with observations of that line.

#### 3.4.1. Formation of emergent H-line intensity

The emergent intensity is given by the formal solution of the transfer equation:

$$I_\nu = \int_0^\infty S_\nu e^{-\tau_\nu} d\tau_\nu. \quad (5)$$

The intensity contribution function can thus be split into the source function,  $S_\nu$ , an exponential attenuation factor ( $e^{-\tau_\nu}$ ) and the product of the cross-section and the column density of emitters ( $d\tau_\nu$ ). This formal solution can be rewritten as:

$$I_\nu = \int_{z_0}^{z^1} S_\nu \tau_\nu e^{-\tau_\nu} \frac{d \ln \tau_\nu}{dz} dz. \quad (6)$$

Now the integration variable is geometrical height,  $z$ , and the optical depth factors have been reorganized as:  $\tau_\nu e^{-\tau_\nu}$  which has a sharp peak at  $\tau_\nu = 1$  and  $d \ln \tau_\nu / dz \equiv \chi_\nu / \tau_\nu$ , where  $\chi_\nu$  is the monochromatic opacity per volume and thus a measure of the density of emitting particles. This last factor is thus important when there are many emitting particles (large  $\chi_\nu$ ) at small optical depth (small  $\tau_\nu$ ), a situation that typically arises in the presence of strong velocity gradients. It is this factor that is responsible for the asymmetry of the Ca II lines.

In the following series of figures (Figs. 8–12) the formation of the  $H_{2V}$  bright grains is shown in the form of the contribution function to intensity and the factors entering its calculation. The figures all have four panels with the full contribution function in the lower right panel and the three factors above in the three other panels. The functions are shown as grey-scale images as functions of frequency in the line (given as Doppler shift) and height in the atmosphere. The image in the lower right panel is thus the product of the three other images. All panels also show the velocity as a function of height with upward velocity positive (to the left in the figure) and the height where  $\tau_\nu = 1$  (grey line). The top right panel also shows the Planck function (dotted) and the source function (dashed) with high values to the left. In the bottom right panel the emergent intensity is also shown as a function of frequency. The time in seconds from the start of the simulation is shown in the top left panel.

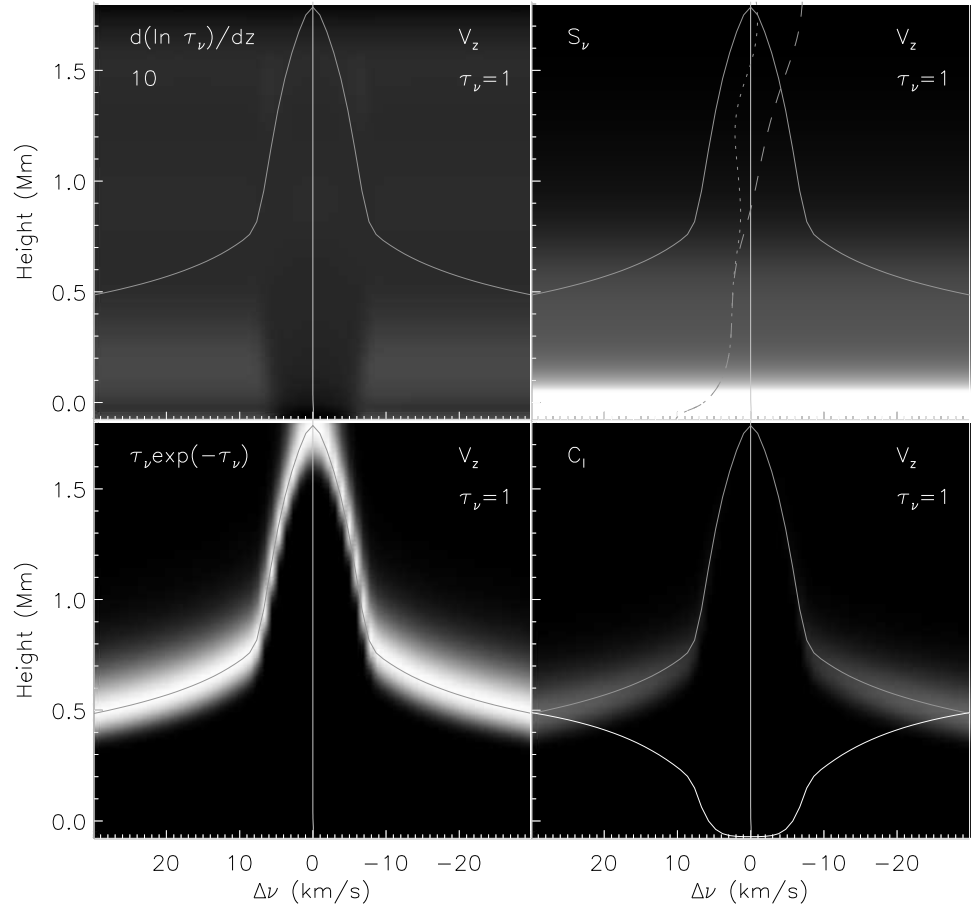


Fig. 8. The formation of the  $\text{H}_2\text{V}$  bright grains is shown in the form of the contribution function to intensity (lower right) and the factors entering its calculation,  $d \ln \tau_\nu / dz$  (upper left),  $S_\nu$  (upper right) and  $\tau_\nu \exp(-\tau_\nu)$  (lower left). The functions are shown as grey-scale images as functions of frequency in the line (given as Doppler shift) and height in the atmosphere. In all panels are also shown the velocity as a function of height with upward velocity positive (to the left in the figure) and the height where  $\tau_\nu = 1$  (grey line). In the top right panel is also shown the Planck function (dotted) and the source function (dashed) with high values to the left. In the bottom right panel the emergent intensity is also shown as a function of frequency. The time in seconds from the start of the simulation is shown in the top left panel.

Figure 8 shows the situation at the start of the simulation before any waves have traveled through the atmosphere. The atmosphere is static and the velocity is zero everywhere. The emergent intensity (lower right panel) shows no emission and all factors entering the calculation of the contribution function are symmetric with respect to line center.

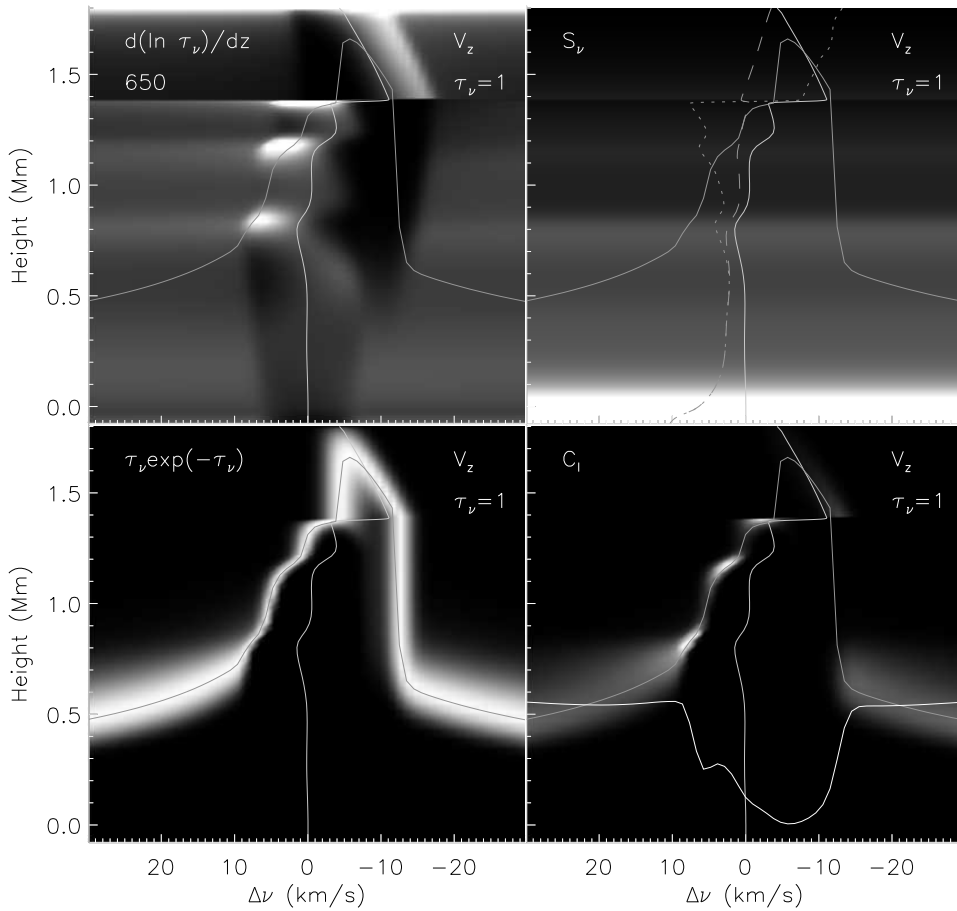


Fig. 9. As Fig. 8 but for  $t=650$ s.

Figure 9 shows the situation after 650 seconds. Several shocks have traveled through, there is one at 1.4 Mm and two waves behind that shock that are steepening. The source function is constant across the line at a given height, (image, upper right panel) because of the assumption of CRD, but is substantially below the Planck function due to the non-LTE decoupling (compare dotted and dashed lines, upper right panel). The  $\tau_\nu e^{-\tau_\nu}$  factor gives weight around  $\tau_\nu = 1$  (lower left panel). The  $d \ln \tau_\nu / dz$  factor gives weight to those depths where we have a velocity gradient such that we have large opacity at a given frequency but a small optical depth (upper left panel). The strongest combined effect is seen where the source function is also large at 0.8 Mm. The absence of a red peak where  $\tau_\nu = 1$  on the red side (at  $-12$  km/s) is due to the lack of opacity there since the atomic absorption profile has been shifted to the blue.

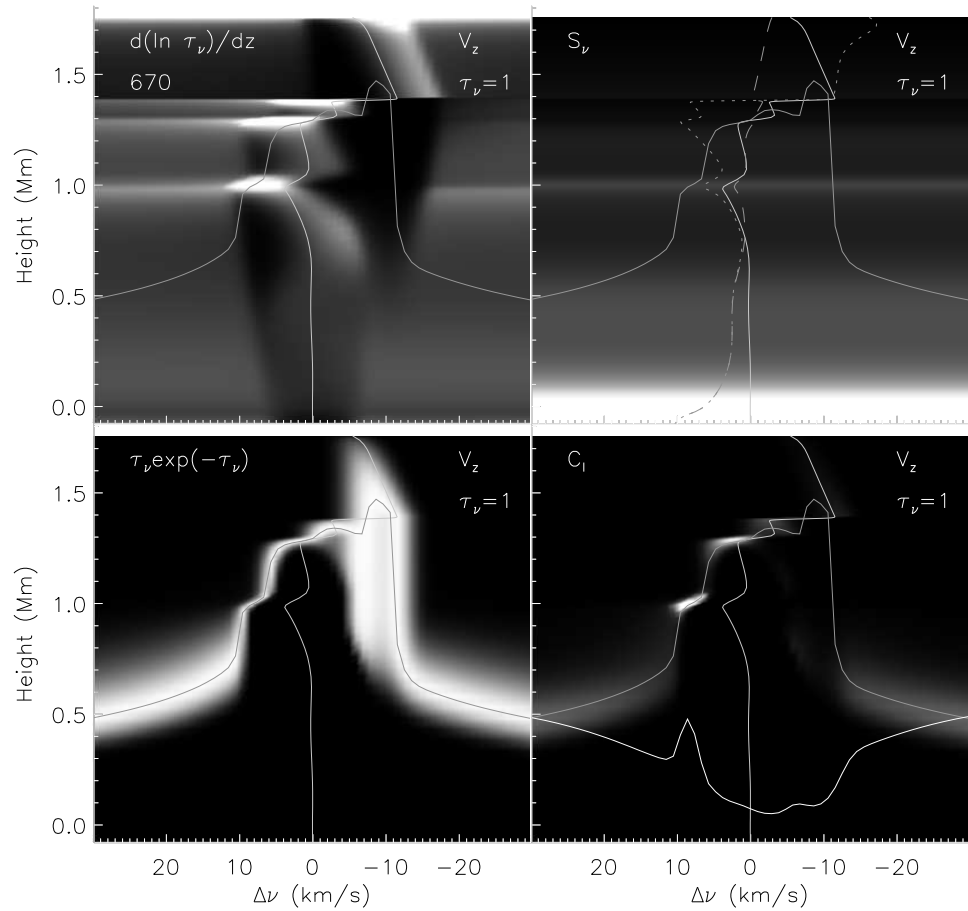


Fig. 10. As Fig. 8 but for  $t=670$ s.

Figure 10 shows the situation 20 seconds later. The upper wave has become a shock and is about to merge with the top shock. Due to the non-LTE decoupling, the source function does not show an extreme maximum at that height and the dominant maximum in the contribution function is from the wave at 1 Mm that has not quite shocked yet. There is a corresponding peak in the emergent intensity profile. The maxima in the upper left panel occurs where we have large velocity gradients, not at the center of the atomic absorption profile but close to  $\tau_\nu=1$ . The distance from line center for the bright emission is thus set by the velocity in the immediate post shock material plus an absorption profile width that is sensitive to the microturbulence.

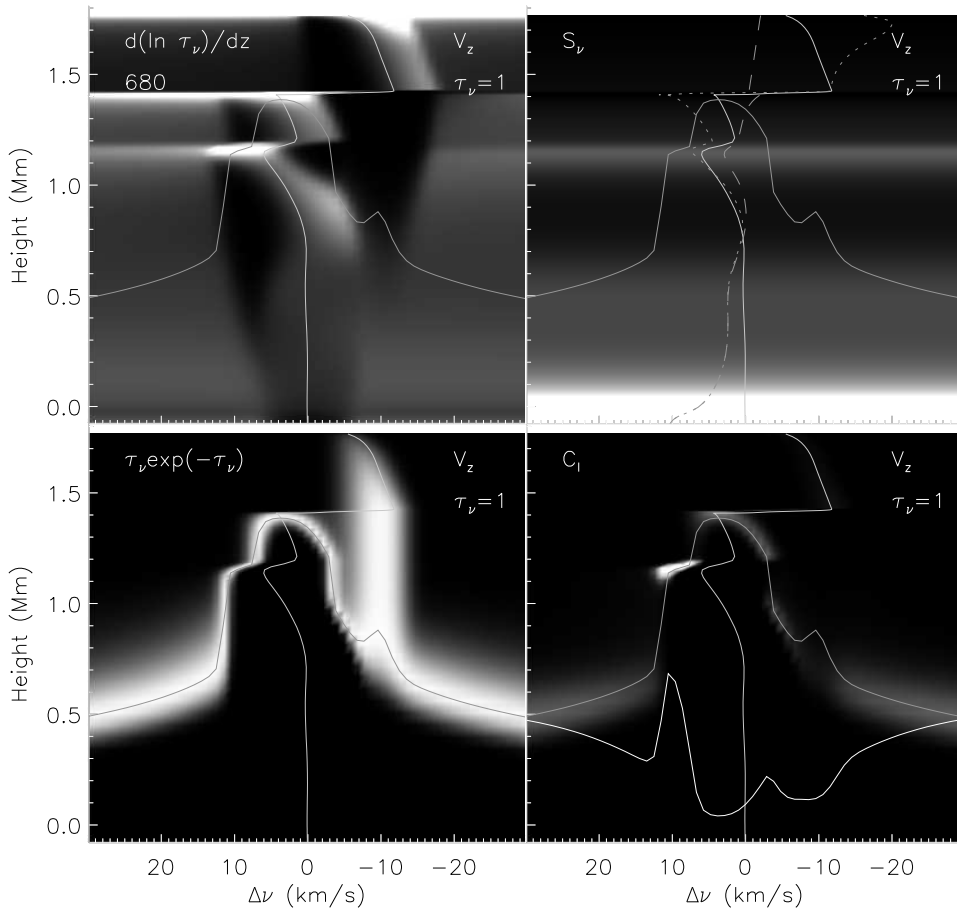


Fig. 11. As Fig. 8 but for  $t=680$ s.

Figure 11 shows the situation 10 seconds later. The two top shocks have now merged into one and the wave behind is steepening into a shock. The  $H_{2V}$  emission comes from 1.2 Mm where the source function has a maximum. The top shock is above the height where  $\tau_\nu=1$  at line center and does not give any emission. There is some emission coming from the line center region where  $\tau_\nu=1$  and there is still substantial emitting matter (top left panel). This emission gives rise to a line core emission peak that with time moves from blue towards red. This is a pattern often found in the simulations that is not clear in the observations.

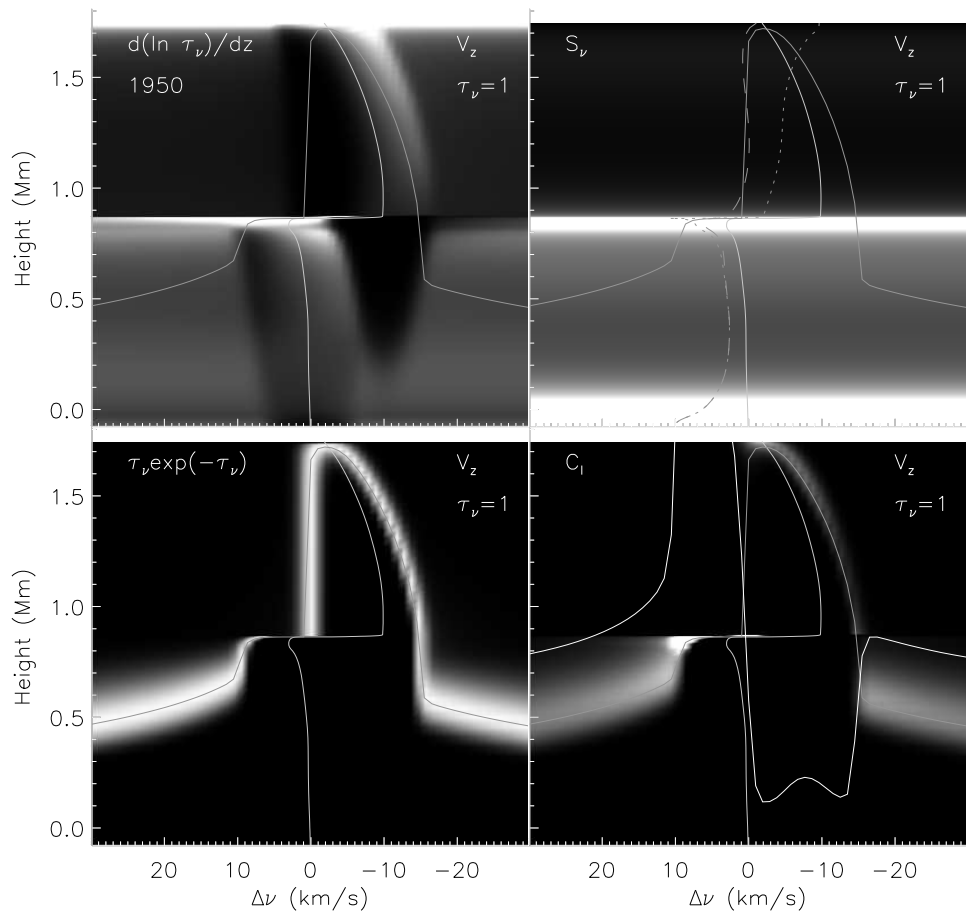


Fig. 12. As Fig. 8 but for  $t=1950$ s. This is the time of the brightest grain.

Figure 12 shows the situation 1950 seconds from the start of the simulation when we have the strongest grain in the simulation. The wake of an earlier strong shock, produced by the merging of several shocks, has created a strong downfall into which another strong shock, resulting from new shock merging, propagates. This creates a strong shock at a low height of 0.87 Mm which produces a large source function as well as a large  $\tau_\nu$  gradient which gives rise to a very strong emission.

To get an asymmetric profile with no red peak thus requires a large velocity gradient at a small enough height that significant numbers of atoms are present. The position of the violet peak is set by the amplitude of the shock plus the width of the absorption profile. The brightness of the peak is set by the shock formation height with lower height corresponding to a brighter peak.

### 3.4.2. Comparison with observations

The piston velocities were chosen to reproduce the measured Doppler shifts in the iron line at 396.68 nm at a given slit position in the observations by Lites *et al.*, 1993. It is then natural to compare the computed behaviour of the H line with these observations. This is done in Fig. 13. The observations are not reproduced in all details but there is a general correspondence down to the level of individual grains. One may identify wing brightenings, periods of weak grains (*e.g.*  $t=900\text{--}1450\text{s}$ ) and strong bright grains ( $t=1450\text{--}2600\text{s}$ ).

The general agreement gives some confidence that the simulations describe the physical processes most important for the bright grain phenomenon. What are the important *discrepancies* between the simulations and the observations and what can be learnt from them? The simulations show a much larger contrast with a sharp transition to a very dark, rather flat core region. There are more details in the core region with frequent secondary maxima. Some of this discrepancy could be due to observational effects. Limited instrument resolution will cause a smearing in the wavelength domain. Scattered light both in the instrument and by the Earth's atmosphere will decrease the contrast and mix in a signal from other spatial positions on the sun. Seeing will also contribute to the total point spread function and in addition introduce a signal from more distant spatial points through image motion.

It is almost impossible to remove these effects from the observations since the various convolutions are poorly known. An additional difficulty with including these effects in 1-D simulations is the unknown spatial correlation. In lieu of a detailed study we just illustrate the effects to be expected by showing the simulation with various degrees of smearing in Fig. 14. Spatial smearing has been simulated by a smearing in the time domain. It is clear that the difference in the form of the profile and in contrast may be entirely due to observational effects. To obtain the maximum information content in the observations one thus has to spend a lot of effort on minimizing scattered light and effects of smearing by seeing.

A more robust difference with observations seems to be a difference in the time when the grains appear. It is possible to make an identification between observed grains and the grains in the simulations but it seems the grains in the simulations appear somewhat later in time (roughly 30 seconds). Note, however, that the piston velocities do not exactly reproduce the Doppler shifts in the iron line; there is a phase difference of 22 seconds. Ideally, the piston velocities should be modified until the iron line observations are matched exactly. To first order that would mean a shift by 22 seconds which would almost remove the discrepancy in the time of the grains.

### 3.4.3. Formation of the grain pattern

When do we get grains and when will there be no grains? We investigate the importance of the piston velocity pattern versus the previous history of the atmosphere by performing a simulation with a 3750 second piston velocity repeated twice. The piston velocity at  $t=3750+t_0$  is thus identical to the piston velocity at  $t=t_0$ . The resulting H-profile as a function of time is shown in Fig. 15. The time evolution has been split into two panels with the right panel showing the second half of the simulation. The piston velocity is thus the same at the same vertical position in

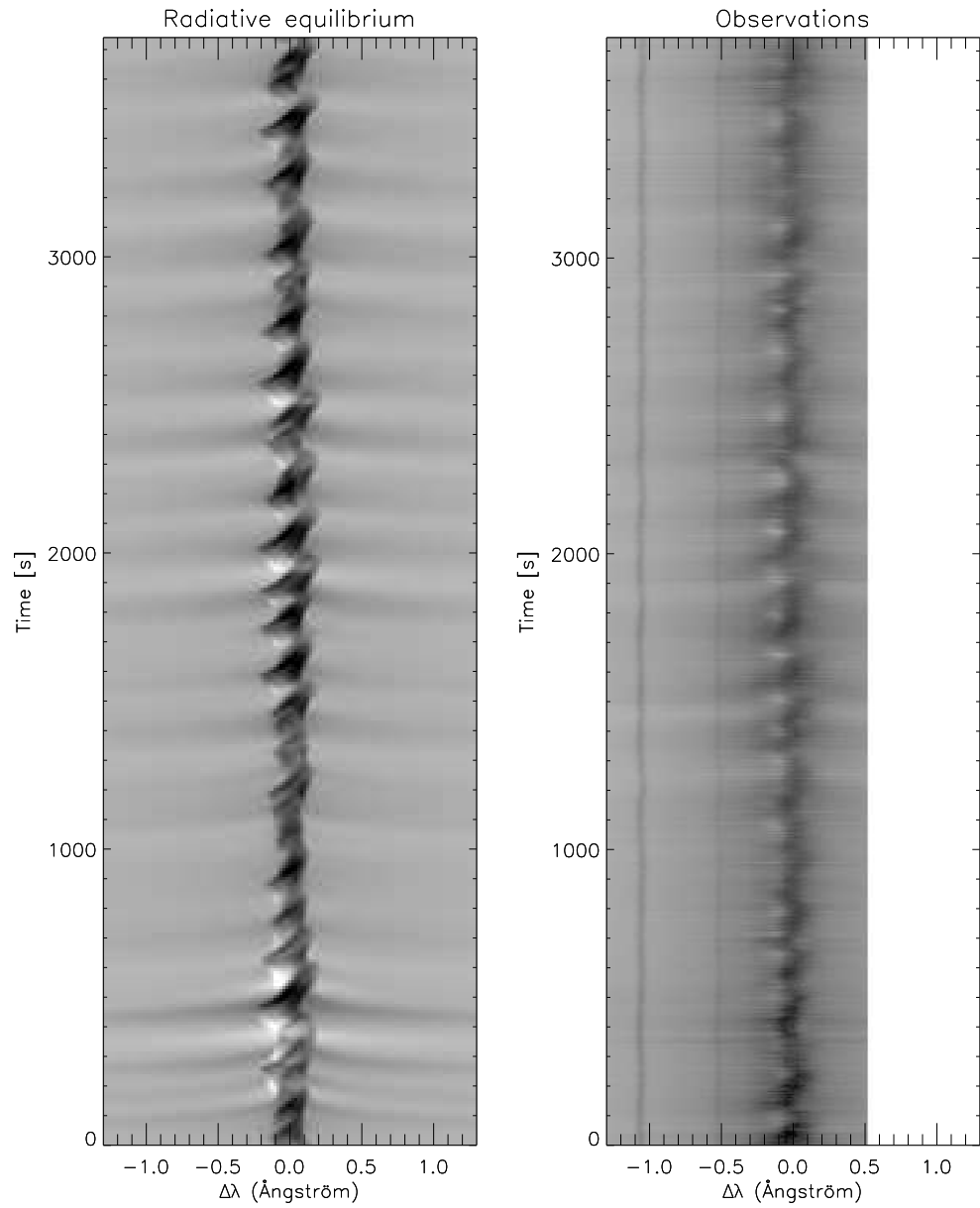


Fig. 13. The computed Ca II H line intensity as a function of wavelength and time compared with observations.

the two panels. It takes some time to set up the typical wave pattern which is the reason why there is little development with time in the beginning. The beginning of the second half of the simulation is also atypical since there is a sudden phase jump when the velocity pattern is repeated. This is also visible in a comparison

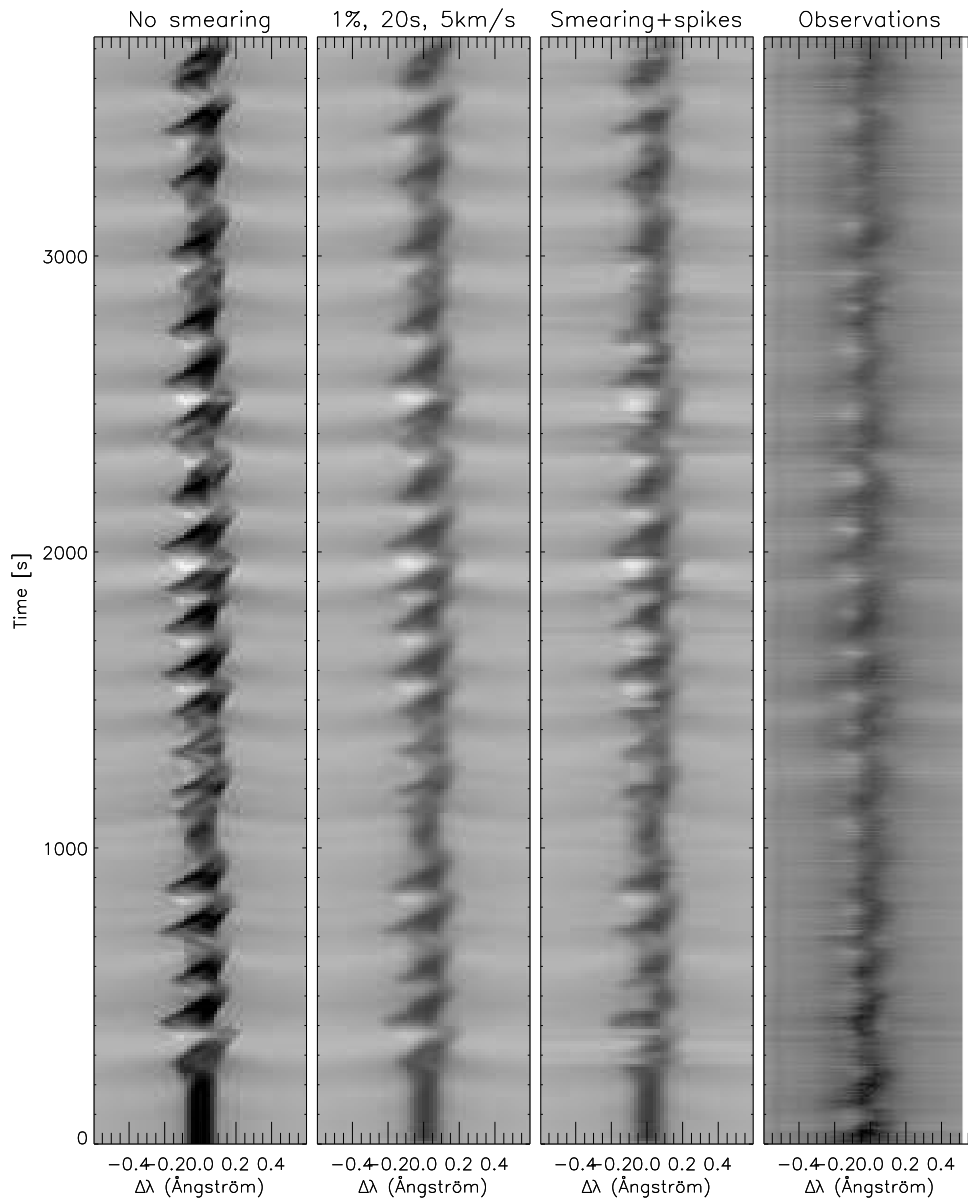


Fig. 14. The computed Ca II H line intensity as a function of wavelength and time compared with observations. The leftmost panel shows the unsmearred results from the simulation. In the second panel the simulation has been convolved with a Gaussian point spread function with FWHM of 20 seconds in the time domain and 0.066 Å (corresponding to 5 km/s) in the wavelength domain. Scattered light amounting to 1% of the continuum intensity has been added. In the third panel image motion has been simulated by shifting the sequence in time with a random function. The same smearing and scattered light as in the second panel was also added.

between the computed velocity at 260 km and the Doppler shift of the iron line: the beginning of the second half of the simulation shows a poor match. Outside these startup periods, the two halves of the simulation show almost exactly the same grain development with no pronounced grains in the time intervals 900–1450s and 4650–5200s and strong grains in the time intervals 1450–2600s and 5200–6350s. We conclude that there is no long time memory in the atmosphere and that the bright grain pattern is completely determined by the velocity pattern.

What in the velocity field is triggering the formation of bright grains? Explanations in the literature go from very high frequency waves (period on the order of 30s) through the process of shock overtaking (Rammacher and Ulmschneider, 1992), three minute waves (Carlsson and Stein, 1992) to five minute oscillations (Kalkofen *et al.*, 1992). To study the importance of propagating frequencies versus evanescent frequencies we have performed two additional simulations where the piston velocities of the full simulation have been either low-pass or high-pass filtered relative to the cut-off frequency at the location of the piston (4.5 mHz). The comparison with the full simulation is shown in Fig. 16. The simulation with only high frequencies in the piston velocities is almost identical to the full simulation after 1600s. In the beginning of the time sequence there is very much increased grain activity. This is due to wave overtaking in the unperturbed atmosphere caused by a few strong spikes in the piston velocity field similar to excitation by velocity impulses (Kalkofen *et al.*, 1992). During the period  $t=1000$ –1450s the high frequency simulation shows more pronounced grains than in the full simulation, the low frequencies modulate the behaviour of the high frequency waves. In the period of the most pronounced grains,  $t=1450$ –2600s, the high frequency simulation shows almost identical behaviour to the full simulation. The low frequency simulation show no grains after the first phase. We conclude that the propagating frequencies are most important for the formation of grains but lower frequency components in the photospheric velocity field modulate the behaviour.

From the analysis of contribution functions (Section 3.4.1) one would expect strong grains to be correlated with large velocity amplitudes around a height of 1Mm. This is clearly shown in Fig. 17 where the velocity as a function of time is shown for eight different heights in the atmosphere. The strong grain at  $t=1950$ s is furthermore shown to be caused by a low shock-formation height (discontinuous rise of the velocity) due to the wave propagating into a region of downfall from previous waves. It is possible to trace back the strong perturbations down to photospheric heights but the picture is not altogether simple. Waves of different frequencies propagate at different phase speeds; at the cut-off frequency the phase speed is infinite and the waves line up vertically, at high frequencies the phase speed approaches the sound speed. These different phase speeds at different frequencies can be seen in the figure as high frequency perturbations appearing at progressively later times with respect to lower frequencies. The interference of these different modes produces the velocity pattern at any given height. When we reach shock forming heights the pattern changes with the whole shock propagating at a supersonic speed. Since the shocks may propagate with different speeds we may get shock overtaking but in general this takes place at heights above the formation height of the grains.

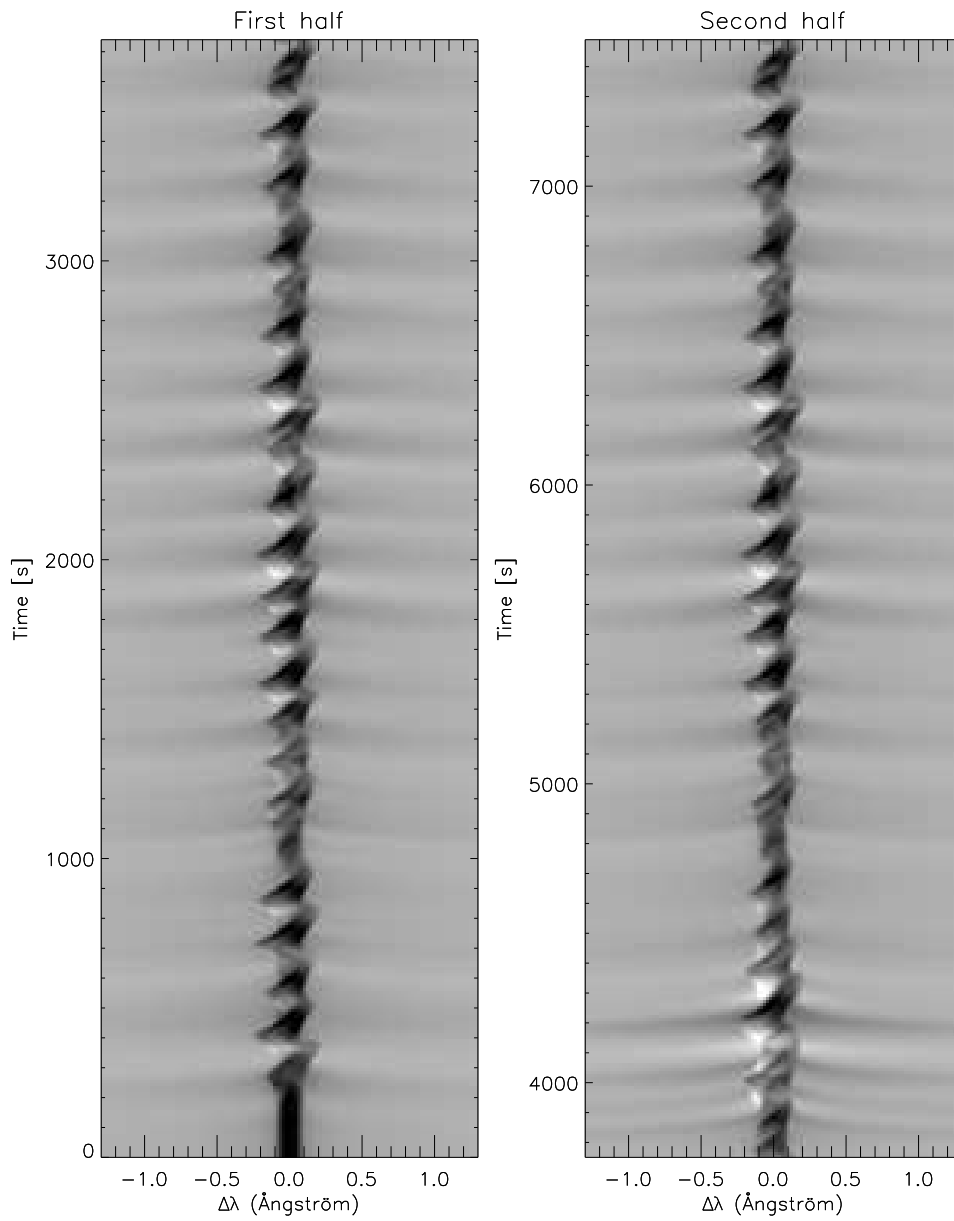


Fig. 15. The computed Ca II H line intensity as a function of wavelength for the full 7500s of the simulation. The piston velocities repeat after 3750s and one vertical position in the two panels thus have the same piston velocity. The pattern is almost identical in the two sections of the simulation outside the first startup periods.

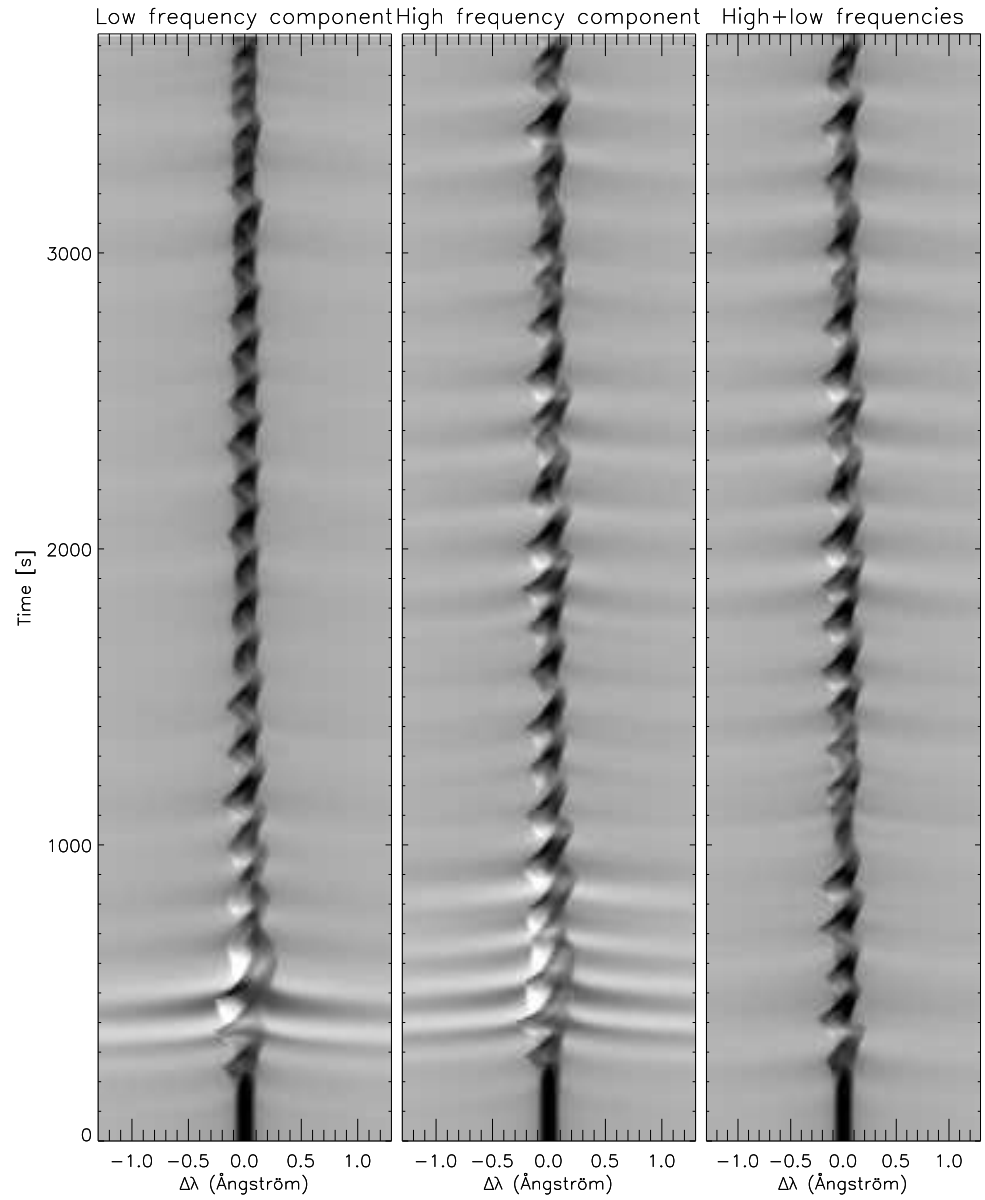


Fig. 16. The computed Ca II H line intensity as a function of wavelength and time for three simulations. The right panel shows the first half of the full simulation while the other panels show simulations where the piston velocities have been low-pass or high-pass filtered at 4.5 mHz. The low frequency component simulation is shown in the left panel, the high frequency component simulation in the center panel.

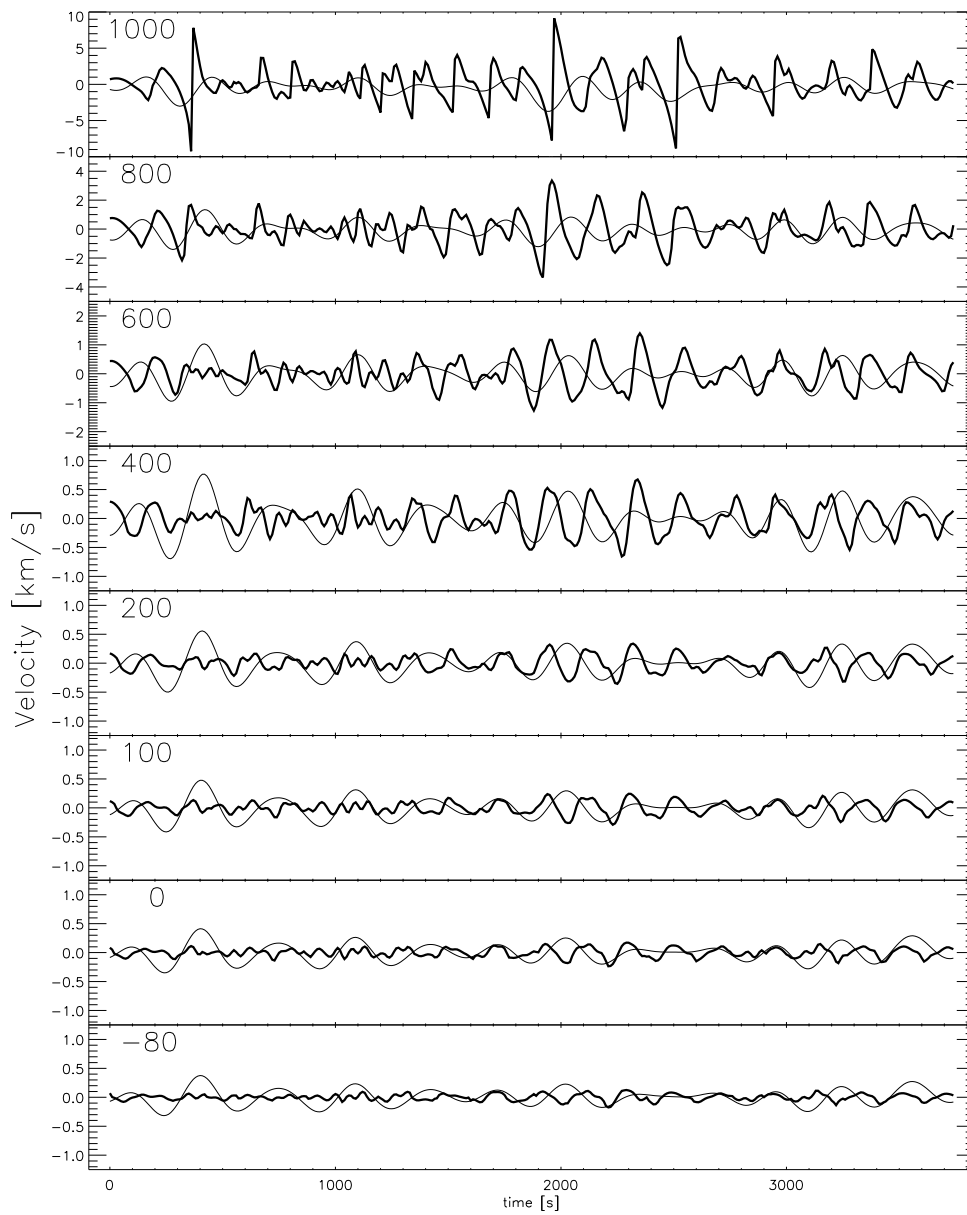


Fig. 17. Velocity as a function of time and height of the atmosphere. The height in km is indicated in the upper left corner of each panel. The velocity has been split into the frequency component below 4.5 mHz (thin) and the high frequency component above 4.5 mHz (thick). The bulk velocity is the sum of the two components. Note that the axis range is different for the top three panels. Strong grains in Fig 15 are clearly correlated with times of large high frequency velocity amplitudes at 1Mm.

#### 4. Discussion

Maybe the most important limitation of the simulations is the 1D restriction of horizontal homogeneity. The energy is forced to travel vertically, there is no radiative loss horizontally and there is no interference between velocities from different spatial points. All these effects can be expected to be important to the physics of the solar chromosphere but a self-consistent non-LTE radiative hydrodynamic simulation in more than one dimension is currently outside the computational possibilities. The observed spatial extent of bright grains is a few arcseconds similar to the total vertical extent of the simulation. A 1D description can therefore be expected to show some resemblance to the real sun, a view supported by the close resemblance of the simulations to observations of high spatial resolution. We thus feel that we can learn something about the real sun from the simulations but warn against over-interpretations.

The simulations aim at describing the non-magnetic internetwork regions of the sun. At some height this distinction between non-magnetic and magnetic regions has to break down with the spreading of the magnetic fields. Such a canopy has not been included in the simulations and for large heights one has to be increasingly careful with comparisons with observations. Reflections from hot material contained in magnetic regions above the internetwork may also influence the non-magnetic regions we aim at simulating.

The simulations were done neglecting the effects of line-blanketing. This will certainly affect the non-LTE statistical equilibrium of our diagnostic continua (UV overionization will be reduced) and the time variation of the radiation temperatures. We do not, however, expect a large effect on the deduced semi-empirical temperature structure based on the fact that both non-LTE and LTE modeling of the diagnostic continua result in the same semi-empirical model atmosphere. The neglect of line-blanketing will also affect the temperature structure in the upper photosphere in the initial model and also the amount of radiative damping and therefore the transfer function of the atmosphere. The neglect of cooling from CO has similar effects.

The transfer function of the atmosphere is furthermore affected by our treatment of the dynamic response of the convective flux divergence. We have assumed a constant convective energy flux divergence per gram on a Lagrangian scale. Based on inspections of 3D simulations of convection (Stein & Nordlund 1993, private communication) this is a reasonable approximation.

The limited numerical resolution will especially affect higher frequencies. The adaptive grid moves grid-points into shock regions but the resolution of waves starting to develop is limited. At the height of the piston the distance between grid-points is 1 km, increasing to 20 km above 300 km height. With ten points per wavelength, this corresponds to a maximum frequency of waves resolved everywhere of 30 mHz, and the numerical resolution should thus not much affect the high frequency waves before they start to shock.

The upper boundary condition aims at being transparent. During the timespan of the simulation, significant mass flows out of the boundary (after 7500 seconds  $4 \times 10^{-4} \text{ g cm}^{-2}$ ). This has been taken into account by increasing the column mass of the top point correspondingly but no effect has been included on the pressure. The mass above the computational domain is thus not supported by the atmosphere in

the simulation. The outflow matter is also assumed to be transparent; no additional opacity is added in. A study of the effects of these assumptions on the results is being carried out.

Complete redistribution (CRD) has been assumed for all transitions. The Ca II H and K profiles will be affected by the neglect of partial redistribution (PRD). Details in the computed profiles, especially peak intensities and the inner wing intensity, should therefore be treated with caution. A proper PRD treatment would involve angle dependent redistribution. Such a study is planned.

Long timescales for ionization/recombination were neglected for all elements not treated self-consistently in the dynamic simulation (all important opacity contributors except hydrogen). One would expect these effects to give increased recombination behind shocks leading to a smaller amplitude for the radiation temperature variations with time. A general increased mean intensity could also be the result giving a higher semi-empirical temperature.

## 5. Conclusions

One main result is that the observed enhanced emission in magnetic field free inter-network regions can be produced by temporally varying waves that generate short intervals of high temperatures, without any increase in the average temperature structure. Because of the exponential dependence of the Planck function on temperature in the ultra-violet, although non-LTE source functions exhibit less sensitivity, these short intervals of high temperature dominate the time averaged intensity. Hence, the radiation temperature represents preponderantly the peaks in the gas temperature rather than its mean value. Because of this non-linear dependence of the Planck function on temperature, the radiation temperature of the mean intensity in the UV is more than the average of the radiation temperature. In addition, non-LTE effects can either increase or decrease the magnitude of intensity fluctuations compared to the magnitude of the temperature fluctuations.

The extra energy that is radiated away in the observed emission comes primarily from the energy dissipated by the wave motions, which goes directly into radiation without passing through a mediating state of enhanced mean thermal energy. The gas pressure work,  $PdV$ , goes primarily into changes in internal energy and gravitational energy.

Significant differences exist between hydrostatic model atmospheres and the average state of a dynamic atmosphere. The contribution function for the intensity in a dynamic atmosphere may be bimodal with one peak around  $\tau_\nu=1$  and another at a shock at smaller optical depth. The mean height of formation will then be between those regions and have no relation to either formation region. Therefore, static formation heights and contribution functions can not be used for analyzing observations of chromospheric continua and lines. The source function is more and more decoupled from the local Planck function the higher in the atmosphere the continuum is formed. This means that the source function shows much less variation in time than the local temperature. Due to the non-LTE decoupling and also because of the width of the contribution functions, the emergent intensity does not show the discontinuous rise signature of shock waves even for the continua formed

where the shocks are strong.

Above the photosphere, the source function is so decoupled from the Planck function that variations in intensity can *not* be taken as a proxy for gas temperature variations. Even in the photosphere such a one-to-one correspondence between intensity variation and gas temperature variation is not possible because the formation height depends on the opacity and therefore on the temperature.

The modification of velocity amplitude and phase as a function of frequency and depth in the atmosphere can be described with a transfer function. This function is rather insensitive to the input velocity field up to heights of a few hundred kilometers but depends on the physics included in the model such as the treatment of line-blanketing and the treatment of the dynamic response of convective energy transport. Evanescent modes are strongly damped while higher frequencies are relatively undamped. By using the derived transfer function it is possible to construct piston velocities that give velocities higher in the atmosphere that match observed Doppler shifts rather well.

The simulations closely match the observed behaviour of CaII H<sub>2</sub>V bright grains down to the level of individual grains. The asymmetry of the line profile is due to velocity gradients near 1Mm above where  $\tau_{500}=1$ . Regions with high opacity and a large source function (and therefore high emissivity) are Doppler shifted to frequencies where there is little matter above to absorb the radiation. The corresponding red peak is absent because of small opacity at the source function maximum. The brightness of the violet peak depends on the height of shock formation; if waves propagate into strongly downfalling matter this formation height may be below 1Mm where the high densities will cause strong emission. The position in wavelength of the bright violet peak depends on the bulk velocity at the shock peak and the width of the atomic absorption profile (described with the microturbulence fudge parameter).

The grain pattern is completely set by the velocity pattern of the piston. When the piston velocity pattern is repeated, the grain pattern also repeats. Both photospheric modes above and below the cut-off frequency influence the grain pattern but photospheric waves around 3 minute period were found to be most important. The grain pattern correlates with the velocity pattern at 1Mm. This velocity pattern is set by interference between different components at lower heights that propagate with different phase speeds until the shock formation heights.

**Acknowledgements.** The discussions at the mini-workshop in June inspired many improvements in the simulations and the computations described in this work were thus carried out after the mini-workshop. Lites and Rutten are thanked for making available their observations. This work was supported by a grant from the Norwegian Research Council and by grant NAGW-1695 from the National Aeronautics and Space Administration. The computations were supported by a grant from the Norwegian Research Council, tungregneutvalget.

## References

- Carlsson, M.: 1986, *A Computer Program for Solving Multi-Level Non-LTE Radiative Transfer Problems in Moving or Static Atmospheres*, Report No. 33, Uppsala Astronomical Observatory
- Carlsson, M. and Stein, R. F.: 1992, *ApJ Let* **397**, L59
- Dorfi, E. A. and Drury, L. O.: 1987, *J. Comput. Phys.* **69**, 175
- Fontenla, J. M., Avrett, E. H., and Loeser, R.: 1993, *Astrophys. J.* **406**, 319
- Gustafsson, B.: 1973, *Uppsala Astr. Obs. Ann.* **5**, No. 6

- Kalkofen, W., Rossi, P., Bodo, G., and Massaglia, M.: 1992, in M. S. Giampapa and J. A. Bookbinder (Eds.), *Seventh Cambridge Workshop on Cool Stars, Stellar Systems and the Sun*, Astron. Soc. Pac. Conf. Series, Vol. 26, p. 543
- Lites, B. W., Rutten, R. J., and Kalkofen, W.: 1993, *Astrophys. J.* **414**, 345
- Mathisen, R.: 1984, *Oslo Inst. Theor. Astrophys. Publ. Series* **1**, 1
- Rammacher, W. and Ulmschneider, P.: 1992, *Astron. Astrophys.* **253**, 586
- Rossi, P., Kalkofen, W., Bodo, G., and Massaglia, S.: 1992, in M. Giampapa and J. M. Bookbinder (Eds.), *Cool Stars, Stellar Systems and the Sun*, Proc. Seventh Cambridge Workshop, Astron. Soc. Pac. Conf. Series, 26, p. 546
- Rutten, R. J. and Uitenbroek, H.: 1991, *Solar Phys.* **134**, 15
- Scharmer, G. B.: 1981, *Astrophys. J.* **249**, 720
- Scharmer, G. B. and Carlsson, M.: 1985, *J. Comput. Phys.* **59**, 56
- Seaton, M. J., Yan, Y., Mihalas, D., and Pradhan, A. K.: 1994, *Mon. Not. R. Astron. Soc.* **266**, 805
- Skartlien, R.: 1994, *Dynamics in stellar chromospheres*, Cand. Scient. Thesis, Inst. Theor. Astrophys. Oslo
- van Leer, B.: 1977, *J. Comput. Phys.* **23**, 276
- Vernazza, J. E., Avrett, E. H., and Loeser, R.: 1973, *Astrophys. J.* **184**, 605
- Vernazza, J. E., Avrett, E. H., and Loeser, R.: 1976, *Astrophys. J. Suppl. Ser.* **30**, 1
- Vernazza, J. E., Avrett, E. H., and Loeser, R.: 1981, *Astrophys. J. Suppl. Ser.* **45**, 635